**The Thesis Committee for Borui Liu**
**Certifies that this is the approved version of the following thesis:**

# Conducting Polymer Hydrogels for High-Performance Electrochemical Devices

**APPROVED BY**
**SUPERVISING COMMITTEE:**

**Supervisor:**

Guihua Yu

Joseph Koo

# Conducting Polymer Hydrogels for High-Performance Electrochemical Devices

by

**Borui Liu, B.E.**

**Thesis**

Presented to the Faculty of the Graduate School of
The University of Texas at Austin
in Partial Fulfillment
of the Requirements
for the Degree of

**Master of Science in Engineering**

**The University of Texas at Austin**
**May 2014**

# Acknowledgements

First of all, I would like to extend my sincere gratitude to my supervisor Dr. Guihua Yu, for his great support in my research life and useful suggestions on my thesis. Also, high tribute must be paid to Dr. Joseph Koo, for agreement in helping reviewing my thesis. I am also deeply indebted to Dr. John Goodenough, Dr. Arumugam Manthiram, Dr. Yu Zhao, Dr. Yongzhu Fu in the study of materials science and engineering and energy storage materials, for their direct and indirect help to me. Special thanks should go to my friends, Mr. Lele Peng, Mr. Ye Shi, Mr. Yu Ding, Mr. Pan Xiong, Mr. Paulo Soares, Mr. Constantine Checkles, and Mr. Vincent Teran, who have put considerable help and time into my research projects and publications. Finally, I am indebted to my parents and parents-in-law, and my lovely wife Mrs. Jiaqi (Kristin) Huang for their continuous support and encouragement.

# Abstract

## Conducting Polymer Hydrogels for High-Performance Electrochemical Devices

Borui Liu, M.S.E.
The University of Texas at Austin, 2014

Supervisor: Guihua Yu

Abstract: Conducting polymer hydrogels (CPHs) is a class of unique materials that synergize the advantages of conducting polymers (CPs) and polymer hydrogels together. It has been employed in many high-performance electrochemical devices for years, such as energy storage and biosensors. However, large limitations of applying CPHs into the abovementioned areas have been facing the researcher for a long time, mainly due to the difficulties from complicated materials synthesis and untenable nanostructures for potential applications. The drawbacks of previously reported CPHs have put numerous disadvantages onto their applications, partially because they have, for example, high prices, untunable microscale or nanoscale architectures, environmentally hazardous properties, and unscalable and time-consuming synthesis processes. In this thesis, we proposed a novel route for carrying out CPHs by one-step organics synthesis at ambient conditions. The CPHs have hierarchically porous nanostructures crosslinked in a three-dimensional (3D) way, which enable its stable mechanical, unique chemical and physical properties, and outstanding electrochemical properties for potential applicability in long-term energy storage devices and highly sensitive biosensors. With highly controllable nanostructures of the CPHs, our novel concept and material system could possibly be utilized in a broad range of electrochemical applications, including but not limited to lithium-ion batteries (LIBs) electrodes, electrochemical capacitors (ECs), biofuel cells, medical electrodes, printable electronic devices, and biosensors.

# Table of Contents

# List of Tables

# List of Figures

# Chapter 1: *Introduction*

Hydrogels are a class of materials that are developed by polymeric chains crosslinking three-dimensionally, which enables flexible property that is similar to naturally produced tissues and can swell under certain conditions but will not dissolve in water. A general concept of hydrogel could be made up of hydrophilic polymeric fibers and up to 99% water held inside the three-dimensional (3D) hydrogel matrix, which enhances their physical stability and flexibility. The highly adsorbing nature, large surface areas and porosities, fast chemical and mechanical responses, stable chemical and electrochemical stabilities, environmental friendliness and cost-efficiency of hydrogels enable them to be very promising alternative candidates for the next-generation electronic and electrochemical materials and devices, such as lithium-ion batteries (LIBs), supercapacitors (SCs), fuel cell electrodes, biosensors, drug delivery, medical electrodes, and so on.[1]

Due to their unique 3D micro-/nano- structures and tunability, hydrogels are else employed as frameworks for combining with other lower dimensional materials, such as micro-/nano- particles (zero-dimensional),[2, 3] carbon nanotubes (one-dimensional),[4] graphene nanosheets (two-dimensional),[5] to form functional composites. The incorporations of additives or fillers help give largely improved promising performance in contrast to their separated individual candidates. In addition to the advantageous characteristics, there are also drawbacks of the aforementioned hydrogel composites. On one hand, the prerequisite for a rationally designed hydrogel composite is that the hydrogels and fillers (inorganic or organic) must be chemically and physically compatible with each other. Therefore, selecting well compatible materials with particular hydrogels leaves the difficulty of hydrogel composite synthesis due to less available choices, especially in the case of pursuing high performance of the composite materials. One the other hand, although using surface modifications or treatments can assist the compatibility between the fillers and hydrogels mother matrix, degrading performance may be resulted from even the simplest treatments. For example, it was reported that CNTs were used as fillers to improve the electrical conductivity of the CNTs/hydrogel composite product. CNTs are known to be hydrophobic, while the hydrogels are hydrophilic. To gain an eventually well compatible hydrogel composite material, CNTs was treated with strong acid to make them to be water-loving materials. However, the acid treatment time and the acid concentration must be strictly controlled, since more than enough treatment can cause degradation or lose of the initial good electrical conductivity, resulting in a non-functional CNTs/hydrogel composite material. Moreover, the complexity and uncertainty in materials synthesis process make them to be of high time-cost and low scalability. Therefore, achieving hydrogels or hydrogel composites of excellent electrical and electrochemical properties without any complicated synthesis is a critical goal for extending their applicability in future electronic devices.

Conducting polymers (CPs), such as polythiophene (PTs),[6] polyaniline (PAni),[7] polypyrrole (PPy),[8] poly(phenylene sulphide-phenyleneamine) (PPSA) and many other synthetic organic polymers,[9] have been widely studied in the past decade. Generally, they are unstable p-type or n-type electrical semiconductors, without introduced anion dopants, which function for charge neutralization and electrical conductivity improvement during polymerization processes. The delocalized π-π conjugated polymer backbone chains are chemically, electrochemically and physically reversible during the doping/de-doping process. Moreover, the anion dopants can also play as crosslinkers at particular binding positions on the polymer host chains, to form 3D porous structures.[10]

The facile micro-/nano- structural building route provide a tunable way to synthesize a series of multifunction materials for advanced electrochemical devices and biomaterials.[9, 11-13]

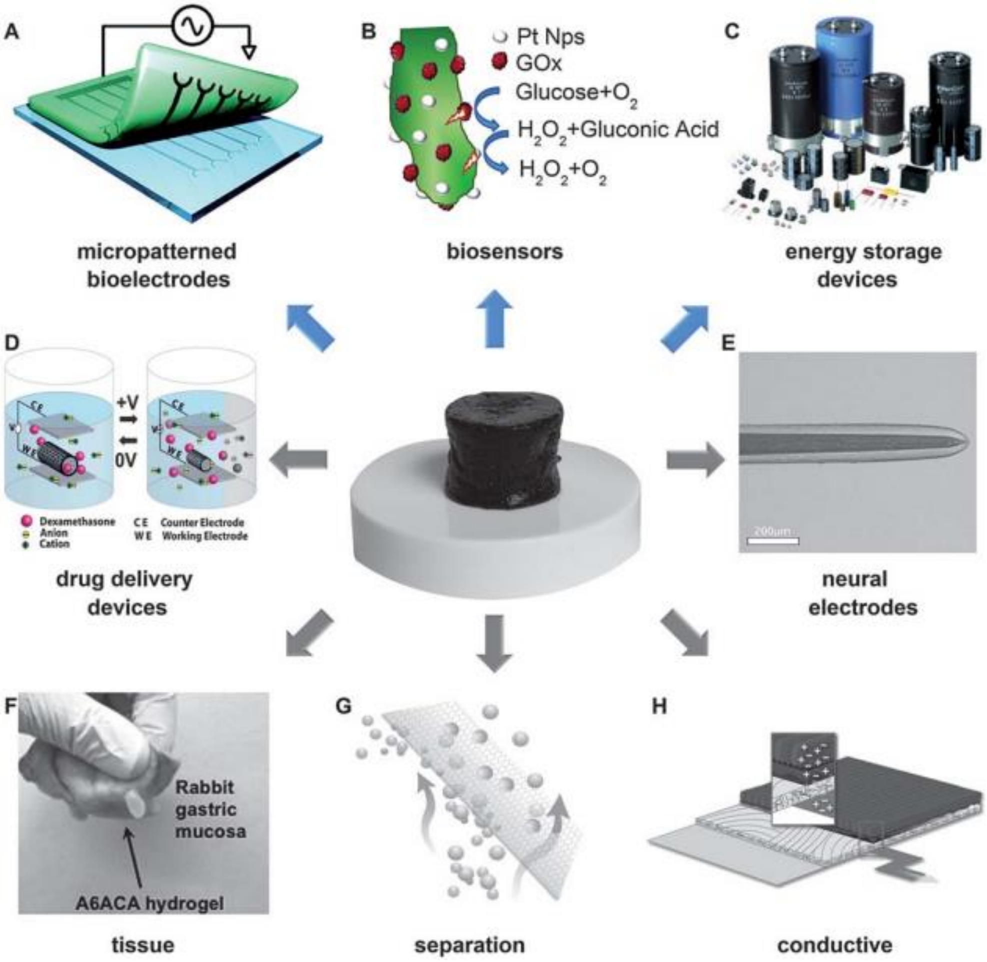

Figure 1: Representative applications of the hydrogels.

Conducting polymer hydrogels (CPHs), as a subgroup of CPs, synergize the virtues of both conducting polymers and polymer hydrogels. The 3D architectures of CPHs not only provide excellent electronic transport pathways through the crosslinked polymeric fibers, but also offer readily ionic migrations due to their large enough porosities. Another key property is the mechanical performance of CPHs. Three-dimensionally built-up polymer framework stabilizes the functional materials and extends their operational life. Another merit of CPHs is their facile processability, which enables CPHs to be cuttable, transformable, and processable by traditional ink-jet printing, electrospinning, screen printing, and newly developed 3D printing methods for micropatterned bioelectrodes, highly sensitive biosensors, energy storage and conversion devices, conductive coatings, etc. (Fig. 1)

# Chapter 2: *Synthetic Hydrogels*

## 2.1 CONVENTIONAL METHODS FOR CONDUCTING POLYMER (CPS) SYNTHESIS

Large efforts on studying the chemical synthesis and electrochemical synthesis of CPs have been carried out extensively during the past decade. In most cases, a hard or soft template will be selected for template-direct growth of CPs. Typically applied templates for this purpose include aluminium oxide membranes,[14, 15] polycarbonate (PC) membranes, block copolymers,[16] porous silicate,[17] mesoporous zeolites,[18] carbon nanotubes,[19] and pre-existing nanostructured materials.[20] Hard template offers unique advantages for conventional materials synthesis. On one hand, they have cylindrical or spherical pores uniformly embedded in the template membranes with a wide range of pore diameters down to 10 nm and with pore densities up to $10^9$/cm$^2$.[21] The templated-based porous nanostructures of hard templates enable precursor fillers to be loaded into the templates and eventually produced with unique nanostructures after removal of the hard templates. On the other hand, most hard templates are commercially available products with controllable pore sizes and distributions, which make it easier for synthesizing the wanted CPs with specified nanostructures. However, challenges are still exist for hard-template based CPs synthesis. Most importantly, hard templates limit the scalability for large-scale fabrications and manufacturing. Also, demanding post-treatment to remove the hard templates for the intermediums in order to get the final nanostructured CPs may complicate the synthesis process and damage the good properties of CPs.

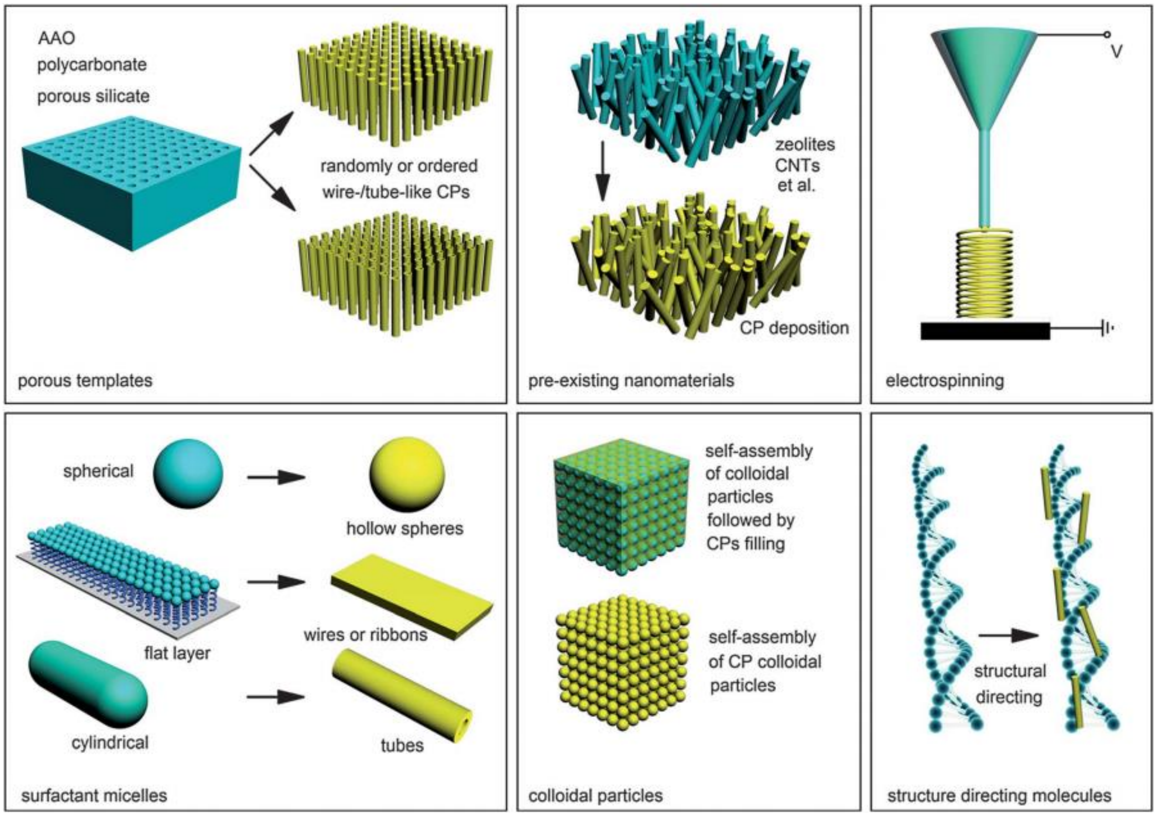

Figure 2: Conventional methods for the synthesis of nanostructured CPs.

Another way of synthesizing CPs is to use soft meso-structured templates such as surfactant micelles, colloidal particles, and structure-directing molecules, etc. Surfactant micelles have been utilized extensively in chemical synthesis of microstructured and nanostructured materials.[22] The fundamental mechanism of surfactant based soft-template synthesis of spatially organized CPs is automatically achieved under certain chemical environment through self-assembly, which is sensitively controlled by the surfactant tail lengths within the hydrophobic cores of the aggregations and effective surface areas composed by surfactant heads facing towards outside of the aggregations.[23] An additional route of preparing nanostructured CPs is to use either conductive or non-conductive colloidal nanoparticles as soft templates. However, the biggest challenge facing these strategies (Fig. 2) is that integration individually existed CPs units into 3D arrangement is practically difficult. Hence, in order to benefit fast matter transfer, namely electronic migration and ionic diffusion, as well as to gain a larger specific surface area derived from high porosity of CPs, alternative approach is critically needed to achieve CPHs.

## 2.2 CONVENTIONAL METHODS FOR CONDUCTING POLYMER HYDROGELS (CPHS) SYNTHESIS

CPHs are highly electronically conductive and structurally integrated hydrogels, with unique nanostructures, large porosity, and reversible electrochemical properties. Conventionally, CPHs are founded by chemical or electrochemical polymerizations of conducting polymer monomers onto non-conductive hydrogel host nano-matrix templates. Using chemical initiators or electrochemical polymerizations, conducting polymer monomers will be polymerized inside the confined nanostructured hydrogel framework. Three major ways of forming CPHs have been developed in previously reported literatures, as indicated by Fig. 3.

First of all, non-templated hydrogel is prepared most commonly. After removal of most of water trapped by the hydrogel matrix, the hydrogel backbones will be established with open nanoporous structures. Then, the conducting polymer monomers will be filled into the ready dehydrated hydrogel matrix, following by a polymerization process of the monomer fillers, as presented in route 1. Route 1 is called "bottom-up" approach. Examples include CP/pHEMA,[24-26] CP/alginate,[27, 28] PEDOT/PAA,[29] PEDOT/PAMPS,[30] and CP/PAAM.[27, 31-34] The second way to synthesize CPHs is to use an already existing template with nanostructured pores or cylinder spaces inside, and then introduce the hydrogel as fillers to fill in the sacrificing template. After removal of the sacrificing template, nanostructured hydrogel will be stably sized into a structurally inverse template, which will be further filled with conducting polymer monomers. Therefore, CPHs will be formed after the finalization of polymerization steps. This is the so-called "bottom-up, up-bottom" approach.[27,35-37] A third way is to first blend hydrogel and conducting polymer monomers together to form a homogenous mixture, and then initiate the polymerization of either component firstly and then the other one afterwards. While, simultaneous copolymerization of both components in the blender of hydrogel and conducting polymer monomers is also an alternative method to achieve the CPHs.[38]

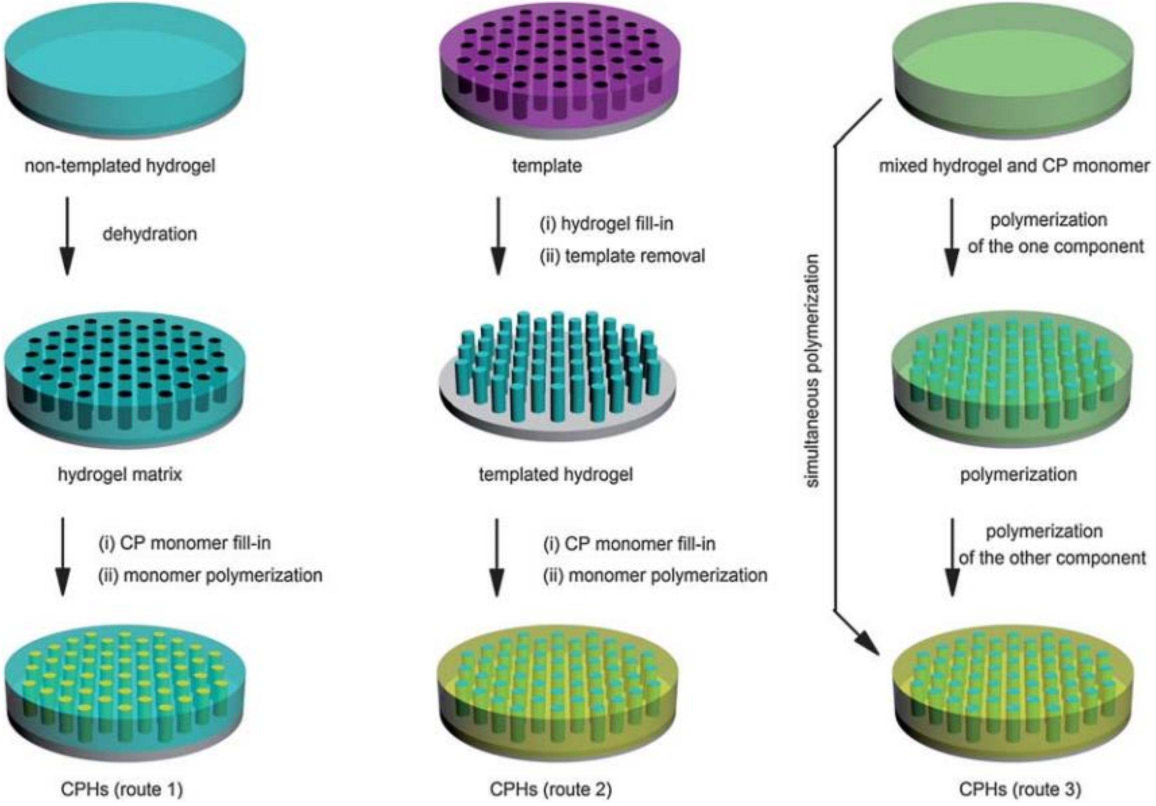

Figure 3: Three conventional methods for the synthesis of CPHs.

It's worth noting that the aforementioned three conventional synthetic routes can only fabricate CPHs composed two physically different and separated components, namely the hydrogels and conducting polymers. Also, all three methods have multiple synthetic steps, which are time-consuming and scientifically intricate. Moreover, secondary processing of the CPHs products, such as purification, tailoring, functionalization, modification and adhibition in potential electrochemical devices, could be largely limited due to the discontinuities, in terms of matter categories and material properties. Therefore, a novel synthesis approach for CPHs with highly integrated physical, chemical, and electrochemical properties is scientifically and technically significant. Here, we will present a new method for CPHs synthesis that is advanced in a facile processability, tunable and integrated nanostructures, excellent electronic conductivity, and outstanding electrochemical activities.

### 2.3 NOVEL METHODS FOR CPHS SYNTHESIS

Basically, conventionally synthesized CPHs could severely suffer from the structural discontinuity, low biocompatibility, and detrimental electrical disintegrity, resulting in the deterioration of the electrical properties. Furthermore, there have been no reports on synthetic CPHs that could be processed or manufactured straightforwardly using large-scale micro-patternings. Phytic acid is a naturally produced saturated cyclic acid, the molecular geometry of which is clearly shown in Fig. 4. The crosslinking effect of phytic acid could be attributed to its six hydroxy groups, which could chemically interact to connect with multiple conducting polymer chains.

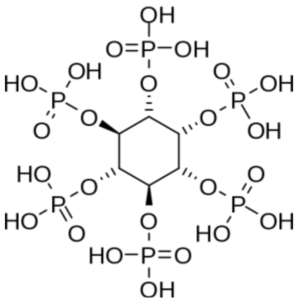

Figure 4: The molecular geometry of phytic acid.

Previously, we reported the nanostructured CPHs of PAni using the abovementioned our novel synthesis.[39] In this synthesis (Fig. 5), the aniline monomer was used as the conducting polymer construction units and phytic acid was used as the crosslinkers. A certain proportion of the mixture of aniline and phytic acid was mixed homogeneously to form a milk-white gel-like solution. After quickly adding in the ammonium persulfate (initiator), the polymerization reactions will be finished soon in several minutes, producing a dark-green hydrogel.

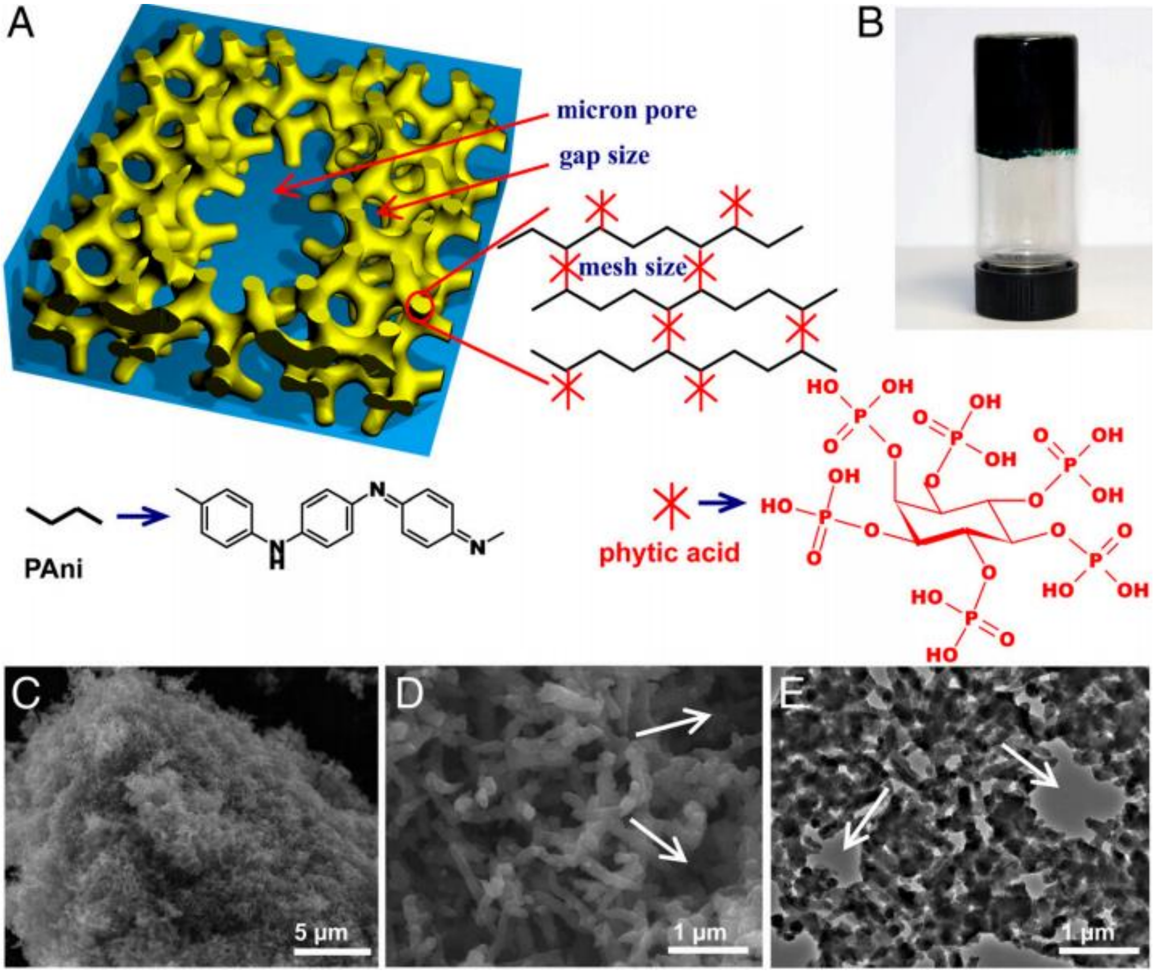

Figure 5: Molecular structures and morphological characterizations of the synthetic CPH of PAni. (A) Scheme of 3D nanostructured PAni CPH. (B) Digital image of PAni CPH product, indicating the excellent viscidity of the hydrogel. (C−E) SEM images of the 3D porous nanostructures of PAni hydrogel.

The PAni hydrogel was tested for micro-patterning using ink-jet printing, demonstrating great processability and scalability. The PAni hydrogel was also tested in an half-cell supercapacitor. The PAni hydrogel-based supercapacitor showed very small electrochemical impedance and good rate performance, indicating good charge transfer capabilities. Additionally, a specific capacitance of ca. 480 $Fg^{-1}$ at a current density of 0.2 $Ag^{-1}$ and 93% capacitance retention over 10,000 cycles were achieved, indicating the excellent electrochemical activity and potential for sustainable energy storage applications. Moreover, the synthetic PAni hydrogel was tested as biosensor electrode. Data showed an obtained response time of only ca. 0.3 s and an average sensing time of ca. 1.1 s, which could be benefited from the 3D porous nanostructures and highly conductive property.

In this view, we herein report several applications of CPHs for energy storage devices and biosensors through a brand novel and forthright synthetic route to achieve 3D nanostructured CPHs networks using conducting polymer monomers as the build-blocks of the 3D conductive network of the hydrogel, and phytic acid molecules as the dopants as well as the crosslinkers.

# Chapter 3: *CPHs for High-Performance Electrochemical Energy Storage (EES) Devices*

## 3.1 3D HYBRID NANOSTRUCTURED ELECTRODE FOR LI-ION BATTERIES

Electrochemical devices using conventionally synthesized CPs, hydrogels, and CPHs have been challenging in future applications, due to the limitation of the traditional multistep synthesis routes and discontinuity of the CPHs properties. Here, we apply our newly developed CPHs synthesis methods of using conducting polymer monomers as the nanostructured hydrogel backbones and phytic acid as the crosslinkers to form 3D porous architectures. The unique 3D porous nanostructured CPHs can not only facilitate ultrafast charge transportation at the interfaces of the aqueous phases and the CPHs as well as inside the CPHs body, but also largely enhance the electrical, electrochemical, and mechanical properties of the CPHs. The improved advantages of the CPHs based on our novel synthesis have been applied in Li-ion battery electrodes, electrochemical supercapacitor electrodes, and biosensors.

Due to the tremendously increasing consumption of reserved fuels (petroleum, natural gases, coal, etc.), and the derived environmental contamination problems, new efficient and long-last energy technologies are immediately needed. Current novel energy sources such as wind energy, solar energy, hydroenergy, and geothermal energy have been contributing to electric power supplies. However, these power sources are still facing unstable accommodation and low efficiency of utilizing energy, due to the frequent fluctuations of electric power transported by the electric grids day and night. In order to improve the electric power source efficiency and accommodate the power shortage at electricity usage fastigium, high-performance energy storage devices are critically needed.

Li-ion battery is widely regarded as one of the most promising energy storage devices, owing to its high energy and power density, high rate performance, no memory effects, long-term cycling lifetime, environmental benignity, and relatively low cost. A Li-ion battery, in general, is composed of a Li-rich cathode, an anode, a separator sandwiched between them, and Li-ion conducting electrolyte wetting all these three components. In a Li-ion battery, lithium ions function as the energy storage charges, and the electrochemical shuttling of lithium ions back and forth between the cathode and anode characterizes the fundamental operational mechanism of the charge/discharge processes. During charge, lithium ions migrate from the cathode side to the anode side, resulting in a step-wise or continuous drop of the cell voltage, and vice versa.[40] Fig. 6 shows the schematic illustration of the structures of a typical Li-ion battery and lithium ions transportations during charge/discharge.

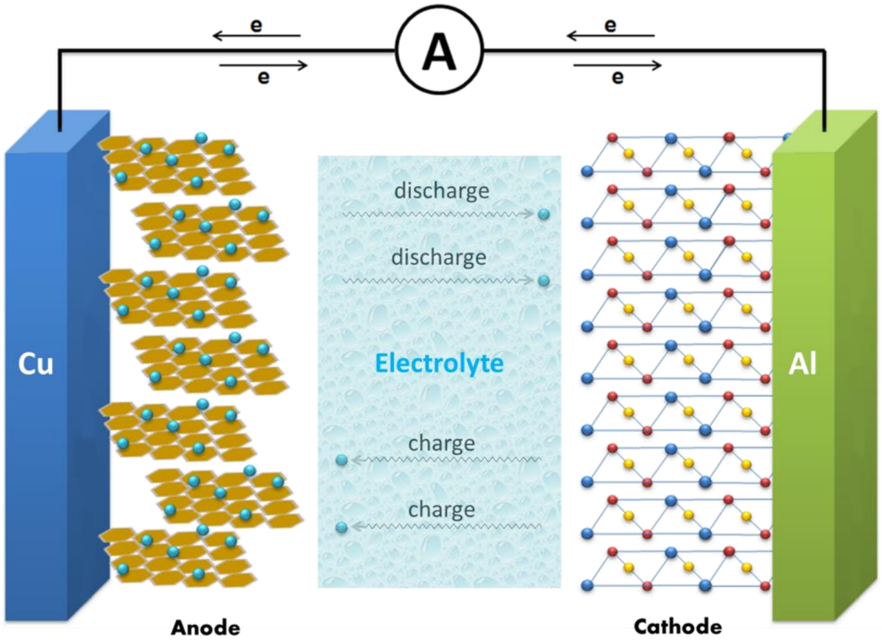

Figure 6: Schematic illustration of a typical battery construction and lithium-ion migration directions during charge/discharge processes.

Recently, silicon (Si) has been intensively studied as one of the most promising anode materials for the next-generation high-performance Li-ion batteries, because: (1) Si has a theoretical gravimetric capacity of ca. 4,200 mAh $g^{-1}$, assuming the formation of $Li_{15}Si_4$ (or $Li_{3.75}Si$) phase via deep charge.[41] This is nearly ten times higher than that of the commercially available graphite based anode materials. (2) Si has a low charge plateau around 0.2 V vs. $Li/Li^+$, which make it possible for a high output voltage of the whole cell. (3) Si ranks the second place out of all elements in the crust, making it an abundant reserve with low cost. (4) Si is environmentally friendly. Even after combustion, Si will produce only silicon oxides, which is much safer, compared to graphitic anodes. However, Si anode is still facing critical problems. First of all, Si has a relative large volume expansion (ca. 300%−400%) during charge, which will cause cracking and pulverization of the Si anode, resulting in electron hopping and larger impedance. Second, Si is intrinsically poor electronic conductor. The low electrical conductivity of Si largely limited the charge/discharge rates and active materials utilization. Moreover, during charge/discharge processes, a layer of solid-electrolyte-interphase (SEI) will be continuously formed on the surface of anode materials. The large volumetric expansion/contraction of Si structures will cause loss of support for SEI layer and break the SEI payer into small pieces into the electrolyte, resulting in a polluted electrolyte and poor cycling. Afterwards, SEI layer will be formed by consuming electrolyte, and will be broke again and again until the battery dies soon. Besides, the kinetics of Si-Li alloying/dealloying during charge/discharge processes are essentially controlled by the Si-Li reacting front. Therefore, nanostructured Si-based anodes are necessarily needed in order to shorten the Li diffusion pathway, boost the utilization efficiency, and to gain high enough cell capacity.

### 3.2 SYNTHESIS OF 3D ELECTRODE FOR LI-ION BATTERIES

Herein, we used our newly developed CPHs synthesis method to form silicon nanoparticles (SiNPs)−PPy CPHs nanocomposite anode materials for high-performance Li-ion batteries, with long-term cycling life and high rate performance, via the following steps.[42] First, solution A was prepared by mixing 84 μL pyrrole monomers (98% reagent grade, Sigma Aldrich) with 184 μL phytic acid solution (50% w/w in $H_2O$, Sigma Aldrich) in 2,500 μL isopropyle alcohol (IPA) to form a milk-white gel. Solution B was achieved by dissolving 274 mg ammonium persulphate (APS) into 2,500 μL deionized (DI) water. Then, 900 μL solution A and 300 μL solution B were mixed well with 60.0 mg SiNPs (MTI, Inc) in a 20 mL glass vial to form a light-brown gel-like blender, followed by 3−5 min bath sonication. Afterwards, the sonicated blender was seated on the lab-table for 10 min, producing dark-green slurry. After 1 min more sonication of the slurry, doctor-blade coating was conducted for the slurry on a piece of copper foil. For comparison, we also synthesized ternary SiNPs−PPy−single walled carbon nanotubes (CNTs) electrode for further improvements in the cycling and rate performance of the battery. The nanostructures of the SiNPs−PPy and SiNP−PPy−CNTs ternary electrodes were characterized by scanning electron microscope (SEM), scanning transmission electron microscope (STEM), and elemental mapping. The electrochemical performance of the two electrode materials were measured by electrochemical impedance spectroscopy (EIS), cyclic voltammetry (CV), rate performance and cycling performance tests.

### 3.3 CHARACTERIZATIONS OF HALF-CELL LI-ION BATTERIES

As shown in Fig. 7, the SiNP−PPy−CNTs nanostructured ternary electrode was synthesized by the one-step organic reaction. The SiNPs were wrapped well in the CPH matrix, and the CNTs were wrapping and crossing the entire SiNP−PPy bulk. The 3D wrapping of PPy CPH on SiNPs could not only enhance the electrical conductivity of the whole electrode, but also largely accommodate the huge volumetric evolution (expansion/contraction) during long-term deep charge/discharge cycling. The CNTs wrapping and crossing can further improve the mechanical and electrical integrity of the SiNP−PPy binary material. Moreover, the PPy CPH and CNTs wrapping on SiNPs surfaces could also stabilize the SEI layer, thus further improving the cycling life for the battery. Additionally, there is an in situ polymeric layer on the SiNP surface, resulting in an enhanced electrical and structural integrity. The synthesis of binary nanostructured SiNPs−PPy electrode was conducted under the same way except for the coating of CNTs.

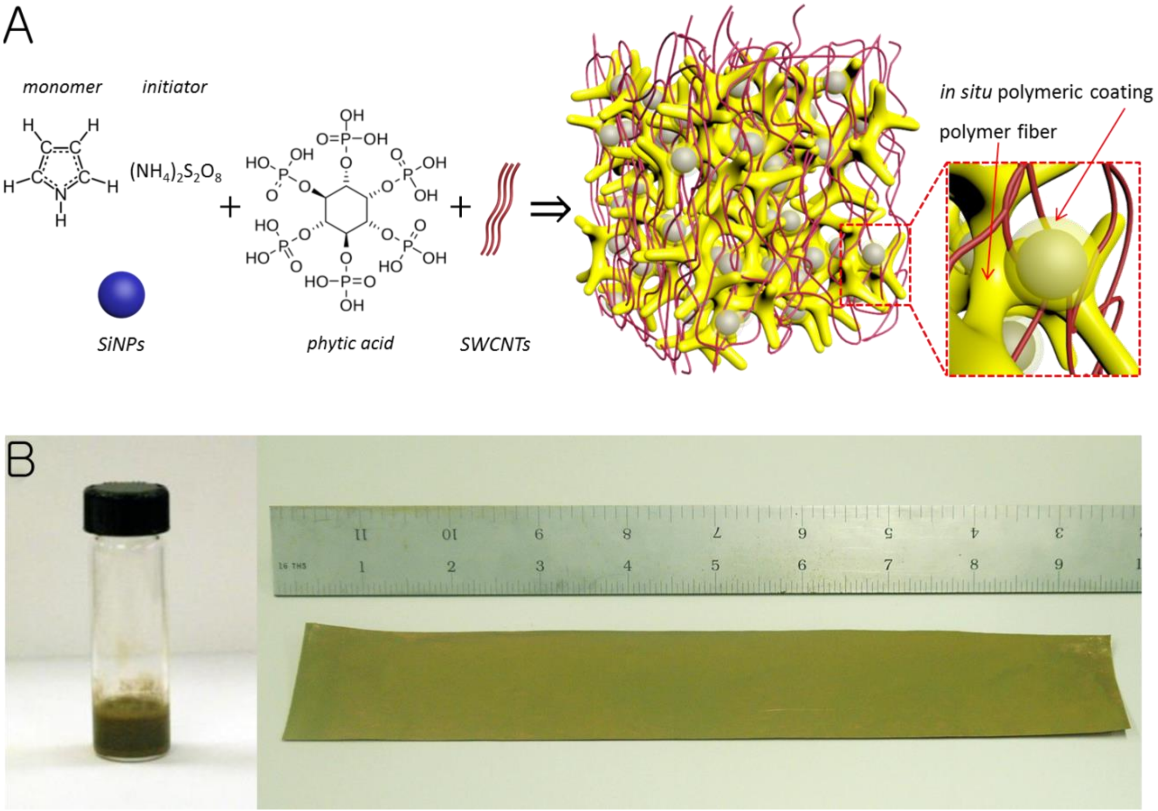

Figure 7: Ternary electrode structure design and fabrication. (A) Schematic illustration of the formation of 3D SiNPs−PPy−CNTs nanostructured ternary electrode. (B) Digital

image showed the as-synthesized SiNPs−PPy−CNT slurry to be dark-green color (left), and indicated that the SiNPs−PPy−CNT slurry can be evenly blade-coated onto the large-area copper foil (right).

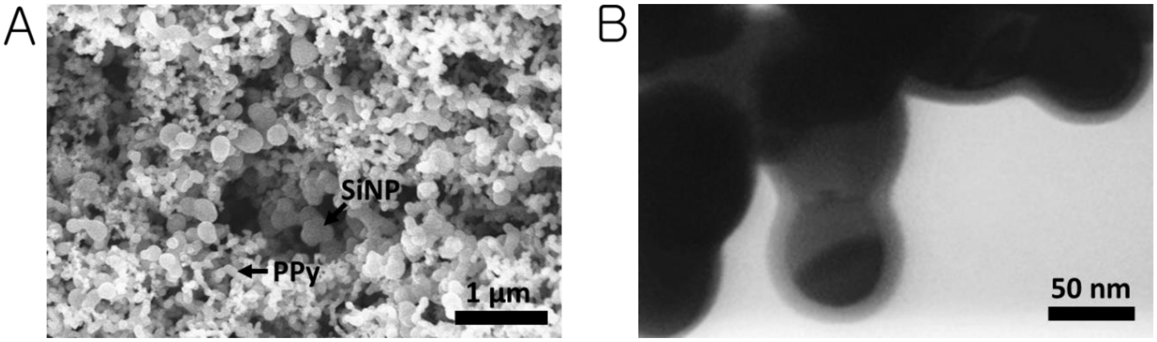

Figure 8: Nanostructural characterizations of 3D Si−PPy electrode.

Fig. 8 presented the nanostructures of binary nanostructured SiNPs−PPy electrode. The 3D hierarchical ternary nanostructures of the SiNPs−PPy electrode were clearly shown in the SEM image in Fig. 8(A). Fig. 8(B) demonstrated an *in situ* layer of polymeric coating on SiNPs surface. Electrochemical analysis tests were carried out in a half cell with lithium metal chip as the counter electrode.

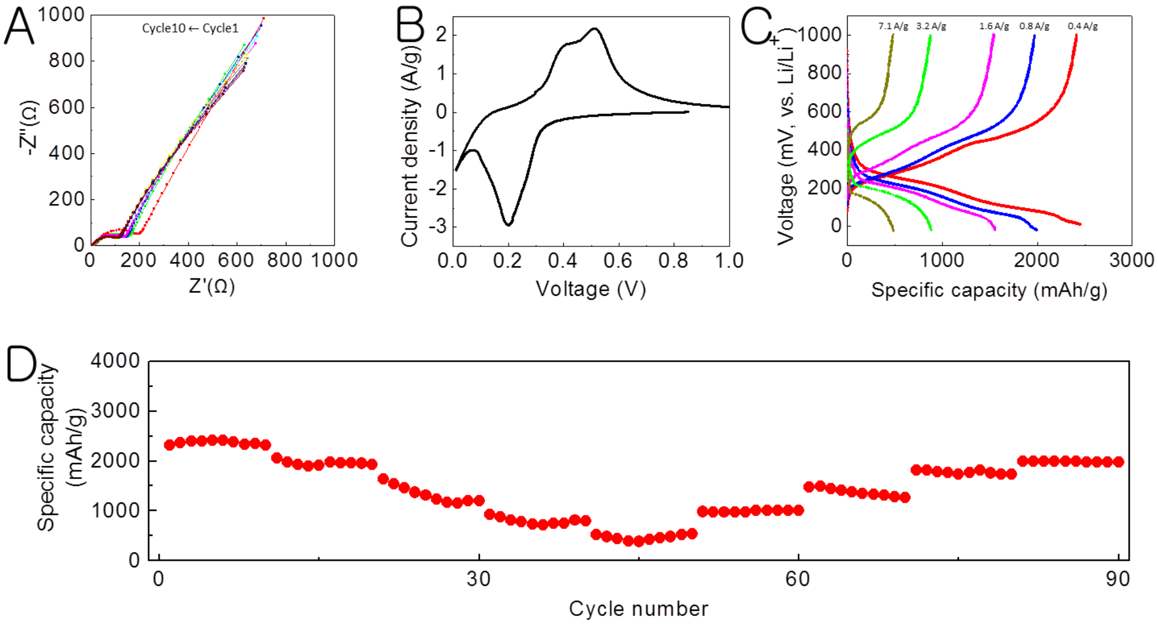

Figure 9: Electrochemical characterizations of 3D Si−PPy electrode. (A) EIS profiles for the first ten cycles. (B) CV profile of the SiNPs−PPy electrode at a scanning rate of 0.1 mV $s^{-1}$ in the voltage range of 0.01−1.0 V vs. $Li/Li^{+}$ after 10 cycles. (C) Voltage profiles at various current rates at 0.4, 0.8, 1.6, 3.2 and 7.1 A $g^{-1}$. (D) Rate performance at 0.4, 0.8, 1.6, 3.2 and 7.1 A $g^{-1}$ rates.

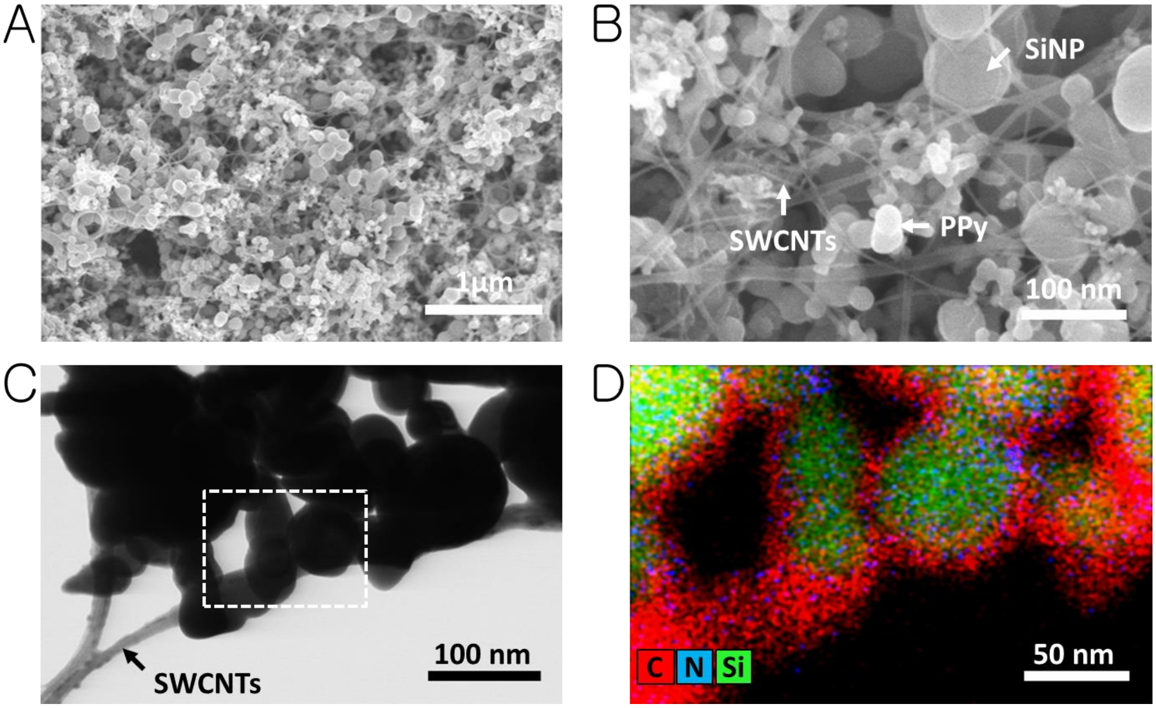

Figure 10: Nanostructural characterizations of 3D Si−PPy−CNT ternary electrode.

Fig. 9 presented the electrochemical performance of the SiNPs−PPy electrode. Fig. 9(A) showed the EIS plots for the first ten cycles of 3D SiNPs−PPy electrode. The impedance for the first cycle was larger than those of the second to the tenth cycles, indicating a decreasing impedance of the of SiNPs−PPy electrode. This could be due to the activation effect and electrical conductivity improvement derived from the Li-Si alloying. Although the SEI layer, which is essentially electronically resistive but lithium-ion conductive, formed majorly during the first charge/discharge cycle, no obvious impedance increase was observed, suggesting a minor negative effect from the SEI formation compared to the former two effects. Also, the impedance of cycle 2−10 had little change, indicating little further SEI formation and good stability of the electrode materials during the cycling afterwards. Fig. 9(B) showed the CV profile of the SiNPs−PP electrode at a scanning rate of 0.1 mV $s^{-1}$ in the voltage range of 0.01−1.0 V vs. $Li/Li^+$ after 10 cycles. Typical redox peaks were observed as one at around 0.2 V and two at 0.4−0.6 V. In contrast to the weak peak at around 0.02 V, the strong peak at around 0.2 V indicated that Li-Si alloying contributed majorly to the total capacity. Charge/discharge profiles in Fig. 9(C−D) showed that the average discharge capacity at 0.4 A $g^{-1}$ rate was ca. 2400 mAh $g^{-1}$, demonstrating the good capacity maintenance at higher current rates of the SiNPs−PPy electrode.

Fig. 10 showed the SEM and STEM images of 3D SiNPs−PPy−CNTs ternary nanostructured electrode. Fig. 10(A−B) clearly showed that the ternary anode material had a hierarchical porous nanostructure. SiNPs were embedded in the highly conductive constructed by PPy CPHs and CNTs. The porous nanostructure and mechanical properties of the ternary electrode can largely accommodate volumetric evolution of SiNPs during Li-Si alloying/dealloying reactions. Also, PPy CPHs plus CNTs can assist the electrical integrity of the electrode material, offering continuous electron transport across the 3D nanostructure to active materials. For Fig. 10(C−D), the STEM image and elemental mapping confirmed an *in situ* polymeric coating on SiNPs surfaces. The *in situ* PPy CPHs coating was intimately formed by the synergistic effect of electrostatic function between the negatively charged −OH groups and positively charged polypyrrole polymer backbone and the hydrogen bonding between phosphoric acid groups in the phytic acid molecules and native $SiO_2$ on the Si particle surfaces. The *in situ* PPy CPHs layer was obviously demonstrated by the carbon signalized area (red) around the SiNPs (green) in Fig. 10(D). The *in situ* PPy CPHs layer could link the individual Si particles to the 3D conductive network, resulting in a further improved electric conductivity of the electrode material. To test the improvement of the 3D Si−PPy−CNT ternary electrode, we conducted similar characterizations as follows.

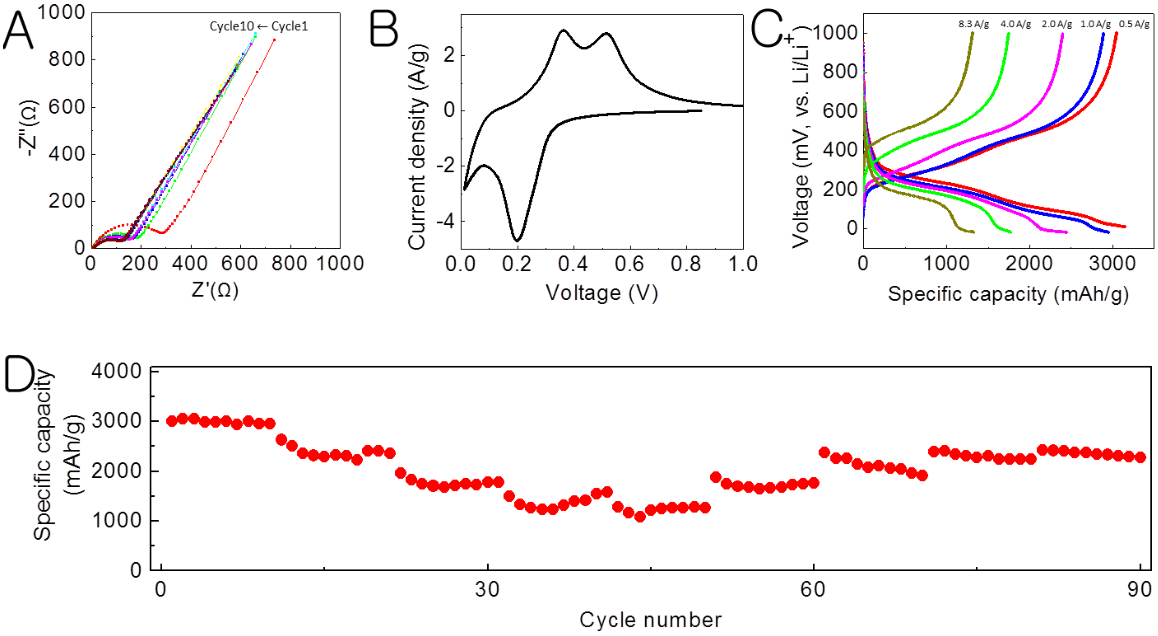

Figure 11: Electrochemical characterizations of 3D Si−PPy−CNT ternary electrode. (A) EIS profiles for the first ten cycles. (B) CV profile of the SiNPs−PPy−CNTs electrode at a scanning rate of 0.1 mV $s^{-1}$ in the voltage range of 0.01−1.0 V vs. $Li/Li^+$ after 10 cycles. (C) Voltage profiles at various current rates at 0.5, 1.0, 2.0, 4.0, and 8.3 A $g^{-1}$. (D) Rate performance at 0.5, 1.0, 2.0, 4.0, and 8.3 A $g^{-1}$ rates.

Fig. 11(A) showed the EIS plots for the first ten cycles of 3D Si−PPy−CNT ternary electrode. The impedance for the first cycle was larger than those of the second to the tenth cycles, indicating a decreasing impedance of the of Si−PPy−CNT electrode. This could be due to the activation effect and electrical conductivity improvement derived from the Li-Si alloying. Although the SEI layer, which is essentially electronically resistive but lithium-ion conductive, formed majorly during the first charge/discharge cycle, no obvious impedance increase was observed, suggesting a minor negative effect from the SEI formation compared to the former two effects. Also, the impedance of cycle 2−10 had little change, indicating little further SEI formation and good stability of the electrode materials during the cycling afterwards. Fig. 11(B) showed the CV profile of the SiNPs−PPy−CNTs electrode at a scanning rate of 0.1 mV $s^{-1}$ in the voltage range of 0.01−1.0 V vs. $Li/Li^{+}$ after 10 cycles. Typical redox peaks were observed as one at around 0.2 V and two at 0.4−0.6 V. In contrast to the weak peak at around 0.02 V, the strong peak at around 0.2 V indicated that Li-Si alloying contributed majorly to the total capacity. Charge/discharge profiles in Fig. 11(C−D) showed that the average discharge capacity at 0.5 A $g^{-1}$ rate was ca. 3100 mAh $g^{-1}$, which was ca. 400 mAh $g^{-1}$ higher than that of the Si−PPy anode at the same current density (Fig. 9).

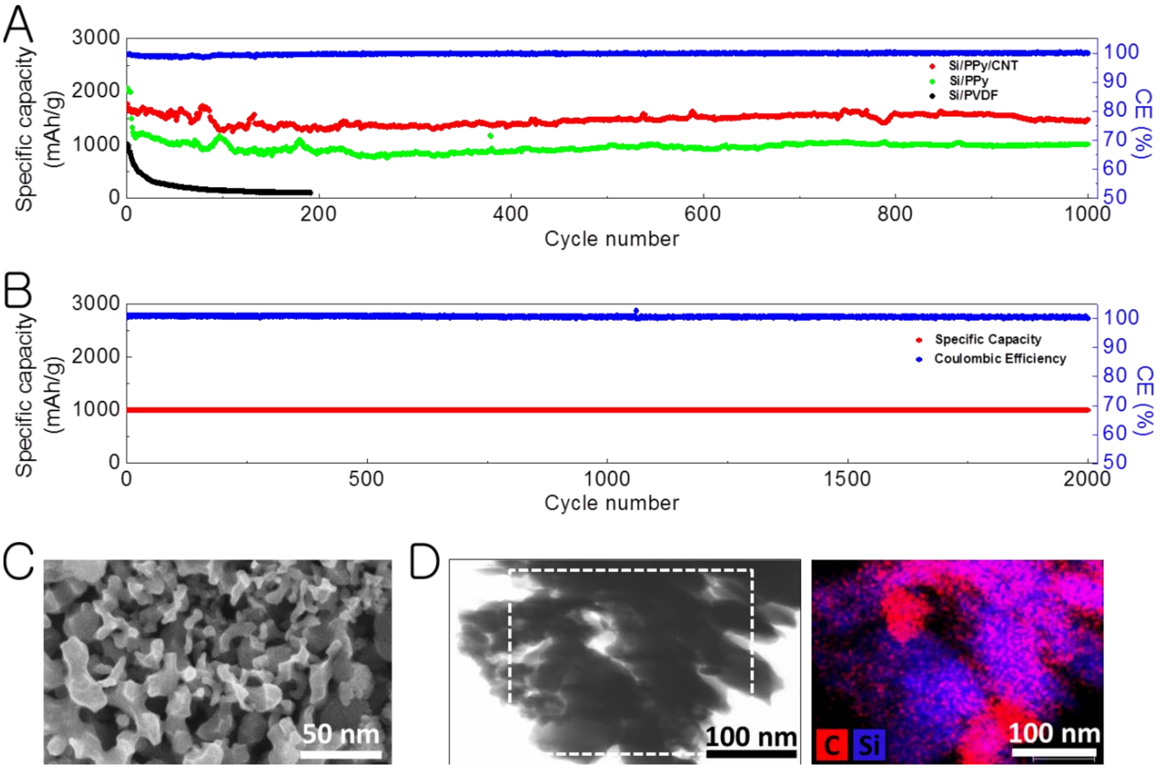

Figure 12: Cycling stability and morphological evolution of the 3D SiNPs−PPy and SiNPs−PPy−CNTs hybrid electrodes after long-term cycling.

Cycling performance tests for the 3D SiNPs−PPy, SiNPs−PPy−CNTs hybrid electrodes, and SiNPs−PVDF regular electrode (control sample) were conducted in the voltage range of 0.01−1.0 V vs. Li/$Li^+$. Fig. 12(A) presented that the 3D SiNPs−PPy and SiNPs−PPy−CNTs nanostructured electrodes showed stable cycling with capacity retentions of over 85% and 60% for 1000 cycles, respectively. The specific discharge capacities of both electrodes were over 1000 mAh $g^{-1}$ at 3.3 A $g^{-1}$ current rate. In sharp contrast, the SiNPs−PVDF regular electrode will almost die in 200 cycles with average capacity lower than 500 mAh $g^{-1}$. The good cycling performance of the PPy CPHs based 3D nanostructured electrodes can be attributed to the mechanical accommodation effect of polymeric hydrogel matrix on volumetric changes of the SiNPs. The high active materials utilization efficiency of the hybrid electrodes were attributed to the 3D electron transfer pathway and the ultrafast lithium ion diffusion crossing the 3D hierarchical porous nanostructures of the hybrid electrodes. It is worth mentioning that the CNTs contributed to a higher specific capacity in the ternary electrode. This could be attributed to the better electric connections between the SiNPs and the outside CPHs network, which offered a smoother transport for electrons and improved utilization efficiency of active materials (Si). Moreover, the Coulombic efficiencies (CEs) of both hybrid electrodes were higher than 78% for the first cycle and over 99% in average for over 1000 cycles, indicating excellent reversibility of the battery. The stable reversible Li-extraction capacity and CE vs. cycle number for the ternary electrode at 8.6 A $g^{-1}$ current rate with discharge capacity limited to 1000 mAh $g^{-1}$ was shown in Fig. 12 (B). The CE was ca. 76% for the first cycle and rapidly ramped to over 99% for the subsequent cycles.

Fig. 12 (C) showed the nanostructures of the cycled hybrid electrode with SEI layer and CNTs removed. After long-term cycling, the 3D matrix was mostly maintained. The fibrous backbones had morphological deformation due to repeated electrochemical lithiation/delithiation. After the cycling, conductively polymeric coating was maintained, which was shown clearly from the elemental mapping in Fig. 12 (D), although little structural changes happened. Therefore, long-term cycling stability could be achieved.

In conclusion, our novel CPHs synthesis method worked well in Li-ion battery. This promising material design and the concept of the scalable synthesis method are expected to be useful for other alloy-type anode such as germanium, tin, and tin oxides.

### 3.4 CPHS FOR ELECTROCHEMICAL SUPERCAPACITORS (SCS)

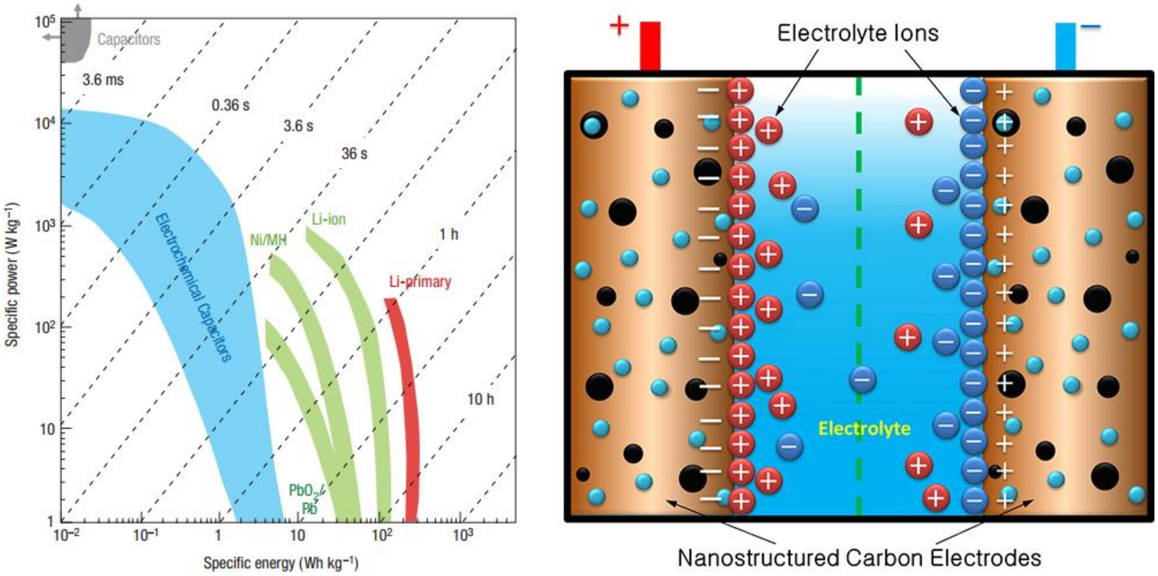

Figure 13: Ragone plot of various electrical energy storage devices and classical constructions of an electrochemical capacitor.

While Li-ion batteries have been used widely studied and applied in up-to-date portable devices, the low current density provided by Li-ion batteries largely limits the power density of the power suppliers and thus the performance of electrical systems.

(Fig. 13) Therefore, electrical power sources that can provide much larger current are critically needed for next-generation high-performance electronic devices. The property differences of Li-ion batteries and electrochemical capacitors are shown in Table 1.[43]

Electrochemical capacitors, namely supercapacitors or ultracapacitors, since the earliest patent filed in 1950's and product marketized in 1970's, have been extensively studied as the most promising backup power suppliers for high-power electrical appliances, such as hybrid electrical vehicles (HEVs), electrical vehicle (EVs), wearable and portable devices. Electrochemical capacitors are generally allocated into two categories: electrical double-layer capacitors (EDLC) and pseudocapacitors. As different from conventional solid dielectric capacitors, these new types of electrochemical capacitors store electricity with two main mechanisms: double-layer capacitance and pseudocapacitance (faradaic charge storage). Moreover, the pseudocapacitance mechanism includes two charge storage principles: redox reactions upon electrosorption or cation intercalation at the electrode surfaces.[44, 45]

Table 1: Comparison of Li-ion batteries and electrochemical capacitors

| Property | Battery | Electrochemical capacitor |
|---|---|---|
| Storage mechanism | Chemical | Physical |
| Power limitation | Reaction kinetics, mass transport | Electrolyte conductivity |
| Energy storage | High (bulk) | Limited (surface area) |
| Charge rate | Kinetically limited | High, same as discharge rate |
| Cycle life limitations | Mechanical stability, chemical reversibility | Side reactions |

Graphitic electrodes for electrochemical capacitors have been commercially used in the past several decades. Mostly, graphitic materials are based on double-layer capacitance mechanism. The excellent electrical conductivity, well stable chemical and electrochemical properties, and good electrochemical activity of graphite/graphene electrodes make them good candidates for capacitive electrode materials.[46-48] However, their applications are narrowed by the limited specific capacitance, which is mainly due to their energy storage mechanism and restricted specific surface area.[49-51] Therefore, many studies have been conducted on combining graphitic materials with transition metal oxides.

Transition metal oxides (TMOs) are famous for their excellent pseudocapacitive property, which offers ultrahigh pseudocapacitance for potential applications. However, most TMOs-based electrodes are intrinsically low electrical conductivity, resulting in poor capacitive performance. Therefore, combining TMOs, such as $RuO_2$,[52-55] $MnO_2$,[56-60] $Mn_3O_4$,[61-63] $V_2O_5$,[64-67] $TiO_2$,[68-71] NiO/$Ni(OH)_2$,[72, 73] *et al.* with graphitic materials seems to be an effective way to provide highenough capacitance and thus accomplish good enough electrochemical performance.[74-78] It has been reported that $RuO_2$ pseudocapacitor electrode has the highest theoretical specific gravimetric capacitance (over ca. 1000 F $g^{-1}$) among all previously reported metal oxides (MOs), but the bottleneck of large-scale application is the high cost (a vehicle-sized EC of $RuO_2$ would cost more than $1 million).[79] Also, $MnO_x$-based electrodes suffer from unwanted dissolving during redox charge/discharge cycling processes.

The specific capacitance ($C_s$) for the device can be achieved using the following the equation:

$$C_s = \frac{4C}{m} = \frac{4I_d t}{V}$$

where $C_s$ is the capacitance of the supercapacitor, $m$ is the total active mass loading on the electrode, $I_d$ is the current density based on mass loading of active materials, $t$ is discharging time, and $V$ is the applied voltage range.

Power density ($P$) and energy density ($E$) can be calculated by using the following equations:

$$P = \frac{V^2}{4Rm} \quad \& \quad E = \frac{0.5CV^2}{m}$$

where $V$ is the applied voltage range, $R$ is the internal resistance, $m$ is the total mass loading of active electrode materials, and $C$ is the measured total capacitance of the supercapacitors.

Flexible electrochemical energy storage devices, such as wearable devices, bendable screens, and foldable televisions, are the most exciting development in the next-generation power sources. Traditional MOs/TMOs based supercapacitor electrode materials used for flexible energy storage devices are facing difficulties such as low active materials loading and decreasing electrochemical performance when aggrandizing the active materials mass density. Therefore, new materials for high-performance supercapacitors with long-last cycling life, ideal electrochemical performance, advanced tunable nanostructures, low cost, high mass-loading density, and scalable manufacturing.

Herein, we report 3D hierarchically porous nanostructured PPy-based CPHs as high-performance flexible supercapacitor electrodes. The organic synthesis of PPy CPHs is generally the same as previously reported synthesis method for PAni conducting polymer hydrogels.[10]

### 3.5 SYNTHESIS OF PPY HYDROGEL ELECTRODE

During polymer synthesis, 274 mg APS solid (98%, Sigma Aldrich) was dissolved in 500 µL DI water, and labeled as solution A. 84 µL pyrrole (99%, Sigma Aldrich) was mixed into 500 µL IPA, followed by the addition of 184 µL phytic acid (50%, wt. % in water, Sigma Aldrich), and labeled as solution B. After gentle shaking, solution B will become an ivory-white blender. The chemical vials in addition to the A/B solutions were rapidly cooled to roughly 0–4 ℃ using dry ice to slow down the exothermal organic reactions. Right after a ready mix of A and B solutions, a controllable time-dependent dip of a piece of carbon cloth (24-hour surface treatment in 8 M $HNO_3$, 10 mm × 20 mm) into the as-synthesized PPy CPHs was conducted. Electrodes were naturally dried in fume hood at room temperature and purified by immersing them in DI water and IPA for 24 hours. Afterwards, another drying step was repeated for future electrochemical measurements. PPy hydrogels with different pyrrole:phytic acid (Py:PA) ratios of 5:1, 10:1 and 20:1 were synthesized for further optimization and electrochemical testing. It is shown in Fig. 14(A) that the hydrated dark-green PPy hydrogel is well attached to the bottom part of a 20 mL glass vial, indicating the property of high viscosity of the hydrogel. Fig. 14 (B) shows two electrode samples of the PPy CPHs coated on individual pieces of carbon cloth. The active materials mass loading densities are decided by the weight changes of the dried carbon cloth before hydrogel coating and after the coated PPy CPHs totally dehydrated over the coated surface areas. After dehydration of the supercapacitor electrodes, the PPy hydrogel will be tightly staying on the carbon cloth, making sure the physical stability of the electrodes during long-term charge/discharge cycling operation. After dehydration, the spongy 3D porous PPy CPHs bulk was pressed under a 100 g balance weight and maintained the intact morphology, indicating the good mechanical property of the PPy hydrogel.

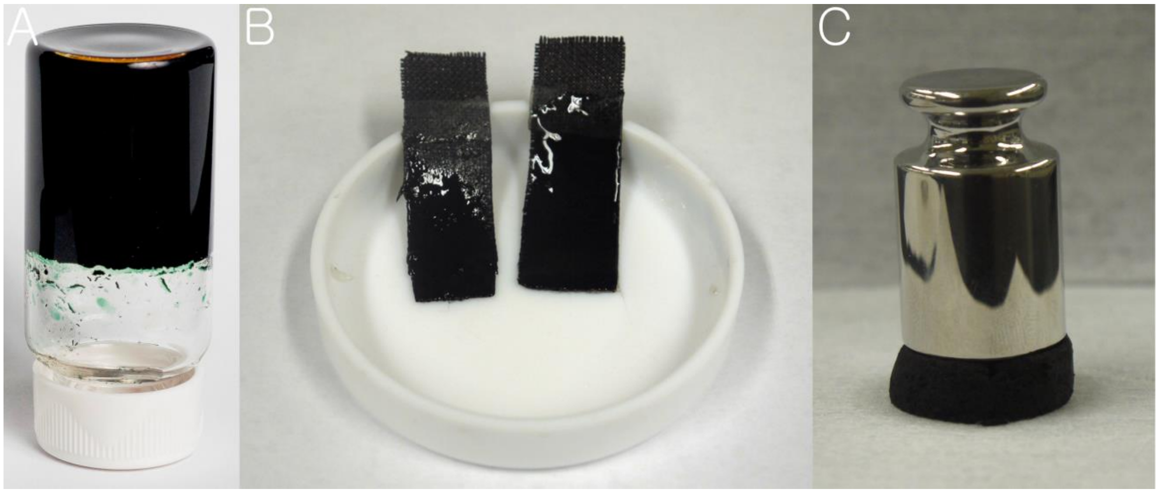

Figure 14: PPy CPHs material and as-synthesized electrodes. (A) Sample of the PPy hydrogel in a 20 mL glass vial. (B) Electrode demos of PPy hydrogel coated carbon cloth. (C) Dehydrated sponge-like 3D PPy hydrogel sample placed under a 100 g weight.

### 3.6 CHARACTERIZATIONS OF HALF-CELL SCS

The Fourier transform infrared spectroscopy (FTIR) analysis in Fig. 15(A) confirms the formation of PPy CPHs. The absorption bands are assigned to the in-ring stretching vibrations of C=C and C−C bonds in the pyrrole rings and stretching vibrations of C=C and C−N bonds (1552.4 and 1704.9 $cm^{-1}$, respectively), C=C and C−N bonds, in-plane and out-of-plane bending vibrations of the C−H bond (1296 and 1045.1 $cm^{-1}$), and stretching vibrations of C=C and C−N bonds (965.4 $cm^{-1}$). These absorptions are characteristics of those for PPy hydrogel.[80] SEM images in Fig. 15(B) show the 3D porous morphology of PPy hydrogel. The foam-like microstructures are constructed by continuous network of spheres with diameter between 200 nm to 5 μm. Further TEM investigation in Fig. 15(C) reveals that the hollow organic PPy microspheres are with shell thickness of 50−100 nm.

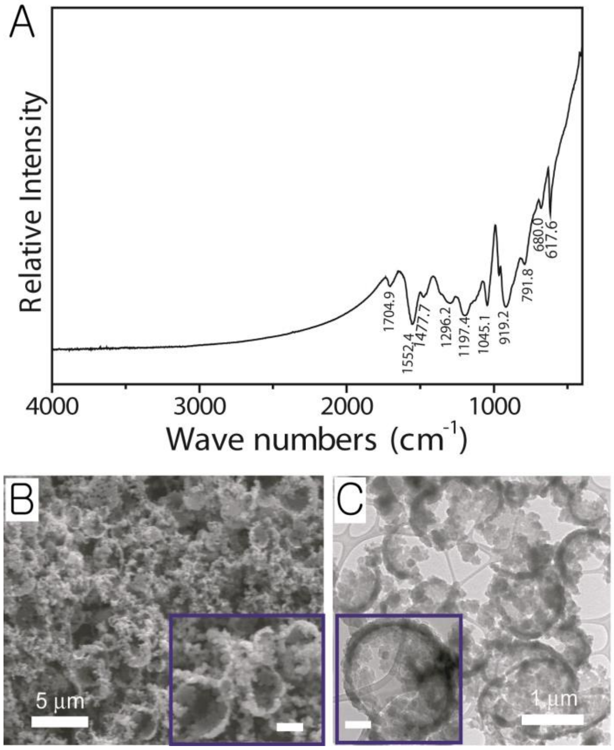

Figure 15: Interconnected hollow sphere conducting PPy hydrogel. (A) FTIR of the PPy hydrogel with characteristic peaks labeled. (B) SEM image of dehydrated PPy hydrogel. Inset scale bar: 1 µm. (C) TEM image of dehydrated PPy hydrogel. Inset scale bar: 200 nm.

EIS, CV, and galvanostatic charge-discharge measurements were conducted for the PPy CPHs electrodes in a conventional three-electrode system. Fig. 16(A) shows the EIS curves of PPy hydrogel based electrodes measured in a 1 M $H_2SO_4$ electrolyte with different PPy mass loadings: 1.8 mg/cm$^2$, 7.2 mg cm$^{-2}$ and 20 mg cm$^{-2}$. The two small semicircles in higher frequency range indicate very small charge transfer resistance. Approximately vertical EIS curve tails in lower frequency range predict idea capacitive ability. Fig. 16(B) exhibits the rate-dependent CV curves at different scan rates of the half-cell PPy hydrogel supercapacitor. The current densities increase along with increasing scan rates, suggesting good rate performance. Fig. 16(C) shows the discharge profiles of the PPy hydrogel electrode at current densities of 0.14, 0.28, 0.7, 1.4, and 2.8 A $g^{-1}$. Specific capacitance vs current density profiles are compared for the hydrogel electrodes with active mass loadings of 1.8, 7.2, and 20 mg $cm^{-2}$ at various current densities in Fig. 16(D), revealing excellent rate capability even with relatively high material loadings. Corresponding data were also shown in form of areal capacitance vs current density in Fig. 16(E). Area-normalized capacitance values are largely improved compared to previous reports.[81, 82] A specific capacitance of 300−400 F $g^{-1}$ was achieved for all the three samples at the current density of 0.2 A $g^{-1}$. To the best of our knowledge, this is the best performance that has ever been reported in literatures compared to that of other supercapacitors using conducting polymers as active electrode materials. Besides, cycle life is another criterion for in supercapacitor operations. Fig. 16(F) shows the cycling stability of the PPy hydrogel electrodes. After 2000 electrochemical cycles, the capacitance degradations are less than 10% for all three samples. High materials loading did not worsen the capacitance retention.

The ideal performance could be attributed to the following reasons. Firstly, the synthesized conducting polymer hydrogel has an intrinsically good electric conductivity along the polymer backbones. Unlike other metal oxide electrodes or composite electrodes, PPy hydrogel electrode has a 3D continuous electron transfer pathway. The highly integrated electronic conductive backbone of PPy hydrogel electrode ensures good electrochemical performance for supercapacitors. Secondly, although specific capacitance (F $g^{-1}$) is commonly used in scientific reports, areal capacitance (F $cm^{-2}$) is more important in practical utilities since it will be restricted by high mass loading. PPy hydrogel electrode has micro-/nano- porous structures. The interspatial porosity offered by ruptured PPy hollow spheres as well as those between PPy nanofibers allows fast ionic migration from the aqueous electrolyte to the electrode inside, favoring rapid adsorption/desorption process. Although PPy hydrogel layer will thicken proportionally with an increasing mass loading, its porous structure can still support high-rate behavior of the supercapacitors. Also, the hydrophilic property of PPy hydrogel can ensure a thorough wetting of the electrode by aqueous electrolyte. Moreover, the unique hydrogel viscosity provides good affinity to the carbon cloth fibers. No obvious active material peeling off from the carbon cloth substrate has ever been observed yet during the electrochemical tests, which physically guarantees enduring stable electrochemical performance of the supercapacitors. Most importantly, the rapidly charged/discharged redox-active sites incorporated on the polymer matrix can increase the overall capacitance of the supercapacitor under fast cycling rates.[83]

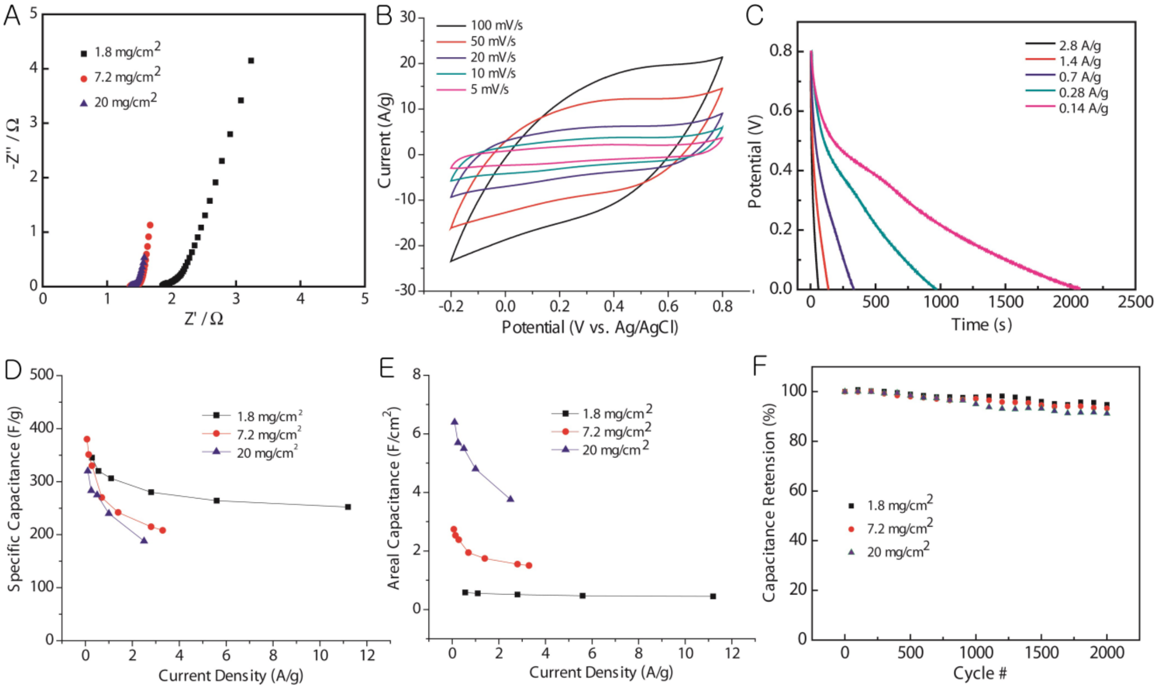

Figure 16: Electrochemical measurements of the PPy hydrogel supercapacitors in 1 M $H_2SO_4$ electrolyte with various high active mass-loadings.

### 3.7 CHARACTERIZATIONS OF SYMMETRIC FLEXIBLE SCS

A highly flexible supercapacitor was assembled by two pieces of dehydrated PPy hydrogel electrodes sandwiching a PVA-$H_2SO_4$ gel-like electrolyte. The PPy hydrogel were well wetted by PVA-$H_2SO_4$ electrolyte. The brief configuration of the solid-state symmetric PPy hydrogel supercapacitor is shown in Fig. 17.

Electrochemical performance of the PPy hydrogel supercapacitor (active mass loading: 20 mg $cm^{-2}$, Py:PA = 10:1) was tested by EIS, CV, rate capability and cycling tests. Fig. 18(A) shows the EIS curve of the symmetric PPy hydrogel supercapacitor. The extremely small values on the real axis in the higher frequency range indicate a good ionic conductivity of the PPy CPHs. The nearly vertical tail in lower frequency range also implies ideal capacitive property of the flexible solid-state supercapacitor.

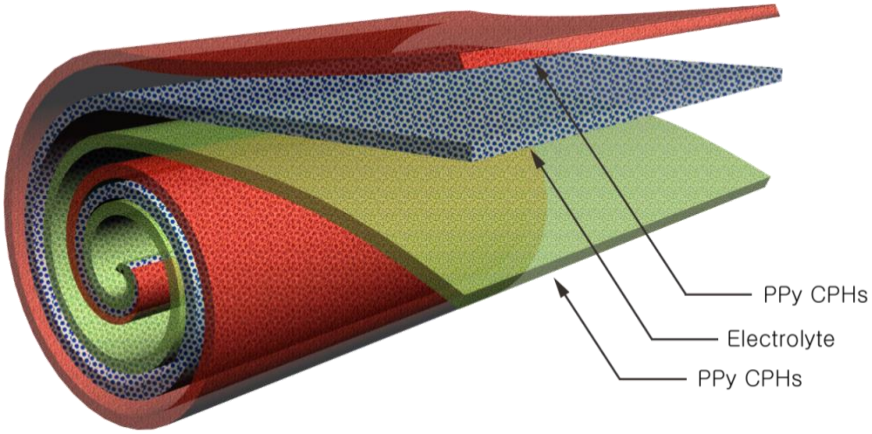

Figure 17: Highly flexible symmetric PPy CPHs supercapacitor.

To test the electrochemical performance under bended conditions, CV was conducted in voltage range of 0.0−1.0 V vs. Ag/AgCl reference electrode (RE) at 100 mV $s^{-1}$ scan rate, showing well overlapping curves with radius of curvatures of ∞, 8 mm, and 3 mm in Fig. 18(B). Apparently, the encircled areas in the closed CV curves decrease as the curvature of the supercapacitor increases. Even under highly bended status, the capacitance degradation is still negligible compared to that of the flat one, which can be attributed to the good mechanical flexibility of the spongy PPy hydrogel network. The porous space enclosed in PPy hydrogel network can largely accommodate the deformation of PPy backbone during bending. To test the flexibility-dependent rate capability, galvanostatic charge/discharge tests were carried out under various current densities. Specific capacitance was calculated and plotted *vs.* current density in Fig. 18(C). The specific capacitance retains ca. 90.1%, ca. 80.6%, and ca. 61.3% of the initial value when current density is increased by 4×, 19×, and 44×, respectively. Cycling performance was further tested for the flexible solid-state supercapacitor by 3000 charge/discharge electrochemical cycles in the potential range of 0.0−1.0 V *vs*. Ag/AgCl RE (Fig. 18(D)). Capacitance retention of ca. 10% was finally achieved, indicating relatively good electrochemical stability and cyclability.

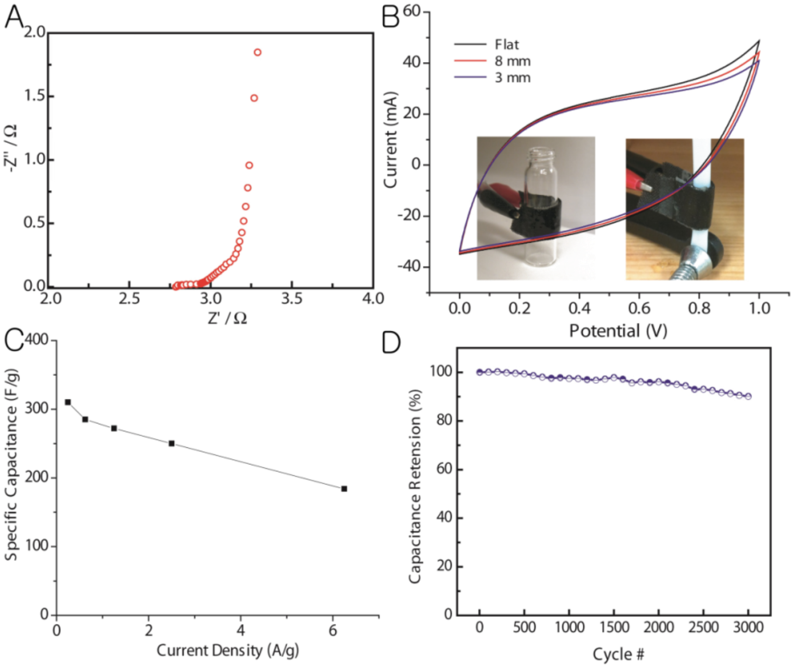

Figure 18: Electrochemical performance of the flexible PPy CPHs supercapacitor under various bended conditions. Inset: radii of curvature of the sample are 8 mm and 3 mm on the left and right, respectively.

In conclusion, the 3D porous nanostructured PPy CPHs achieved by our unique materials synthesis method has demonstrated ideal electrochemical properties for high-performance flexible solid-state supercapacitor electrodes.

# Chapter 4: *CPHs for Glucose Enzyme Biosensors*

Human health is one of the most popular social topics in the past decade. As one of the leading causes of disabilities and death, blood sugar illness has been early brought to the worldwide research forefront. As soon as the blood glucose concentration is higher or lower than theoretically normal range of 80−120 mg $dL^{-1}$ or 4.4−6.6 mM, potential metabolic disorders reflect on human body. With the consumption accounting for about 85% of the whole biosensor market and the critical requirements for a tight monitoring of blood glucose levels, more developed highly sensitive, low-cost, long-life biocompatible electrochemical glucose biosensors are eagerly needed.

## 4.1 DEVELOPMENT OF ELECTROCHEMICAL GLUCOSE BIOSENSORS

Electrochemical glucose biosensor was firstly reported by L. Clark Jr. and C. Lyons of the Cincinnati Children's Hospital in the year 1962. It was established on a glucose oxidase ($GO_x$) thin layer captured over an oxygen electrode via a semipermeable dialysis membrane. The sensing mechanism relied on detecting the oxygen consumed by the enzyme-catalyzed reaction, while applying a negative potential to the platinum (Pt) cathode for a reductive detection of the oxygen consumption, as the chemical reaction equation shown below.[84]

$$\text{Glucose} + O_2 \xrightarrow{\text{glusoce oxidase}} \text{Gluconic Acid} + H_2O_2,$$

and

$$O_2 + 4H^+ + 4e^- \rightarrow 2H_2O.$$

In 1973, G. Guilbault and G. Lubrano carried out an enzyme electrode for the amperometric (anodic) determination for blood glucose.[85] The mechanism was based on the monitoring of the hydrogen peroxide product, as shown by the equation below.

$$H_2O_2 \rightarrow O_2 + 2H^+ + 2e^-.$$

Then, continuous ex-vivo and in-vivo monitoring of blood glucose were put forward, which were proposed by P. Schlapfer *et al.* and M. Shichiri *et al.* in 1974 and 1982, respectively.[86, 87] The 1980s−1990s epoch witnessed the most vigorous growing of biosensor developments, indicating the increasing prominence of biotechnology at that era. Emerging developments and outcomes included mediator-based ‘second-generation’ glucose biosensors, screen-printed strips for self-monitoring, enhanced electrical communication between the redox center of $GO_x$ and the electrode surface, and subcutaneously implantable devices.[88-91]

The third-generation glucose biosensors move towards a much higher selectivity, advantaging in very low operating potentials and the absence of redox mediators. Several works were reported regarding the overcoming of the spatial separation of donor-acceptor pair for a direct electron-transfer route catalyzed by $GO_x$.[92-95] The comparison of three generations of glucose biosensors are presented in Fig 19(A−C). Despite the comforting progresses in the development of highly sensitive glucose biosensors, they are still limited due to not good enough performance.

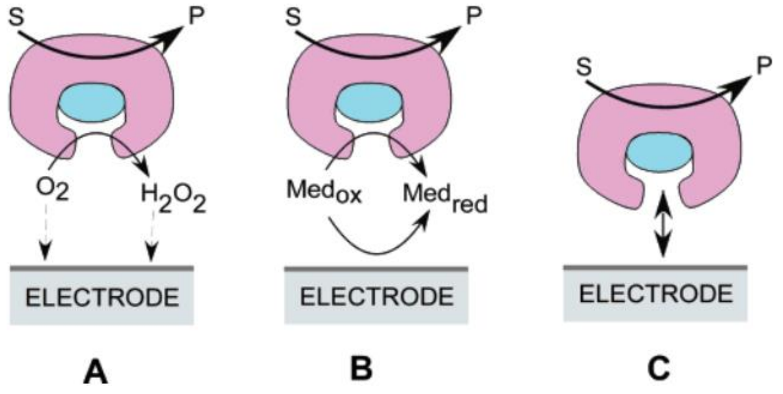

Figure 19: Schemes of the three generations of electrochemical glucose biosensors. (A) Natural oxygen cofactor. (B) Artificial redox mediators. (C) Direct electron transfer between $GO_x$ and electrode.

## 4.2 PANI HYDROGEL FOR HIGHLY SENSITIVE GLUCOSE BIOSENSORS

Next-generation electrochemical glucose biosensors are very important for accurate human blood monitoring and potential disease prevention. However, many glucose biosensors have restricted detective capability dominated by their not fast enough electrical signal direction and transfer. Therefore, new materials with high electrical conductivity, good ionic transportability, high electrochemical activity, good electrochemical stability, as well as good biocompatibility are of critical significance for improving the sensitivity of electrochemical glucose biosensors.

Herein, we report a highly sensitive glucose enzyme sensor based on platinum nanoparticles (PtNPs)−polyaniline (PAni) CPH heterostructures.[96] The PtNPs−PAni glucose biosensor was founded on the platform of our previously reported CPHs synthesis method.[10]

## 4.3 SYNTHESIS OF PTNPS−PANI GLUCOSE BIOSENSORS

Synthesis of the PAni hydrogel: Solution A was achieved by well mixing the blender of 921 μL phytic acid solution in 2000 μL DI water, followed by adding in 458 μL distilled aniline monomer (99%, Sigma Aldrich) and then sonicated to get clear solution. Solution B was achieved by dissolving 286 mg APS (98%, Sigma Aldrich) in 1000 μL DI water. Afterwards, solution A and B were rapidly mixed in a 20 mL glass vial under ice-water bath (0−4 ℃) condition, and a dark-green PAni hydrogel will be formed in 3−5 min.

Fabrication of PtNPs−PAni glucose biosensor: 5 μL mixed solution containing A and B was coated onto a platinum electrode of 5 mm in diameter and ca. 0.1963 $cm^2$ in area. After being transferred to 2 ℃ environment for 10 min, a thin uniform PAni hydrogel layer was formed on the Pt electrode surface. Then, electrode was dipped in DI water at 40 ℃ for 30 min to remove oligomers and excess ions. Afterwards, the PAni hydrogel-modified Pt electrode was immersed into a solution containing 4,500 µL DI water, 9.65 µL $H_2PtCl_6$ (1 mM), and 250 µL formic acid for 12 h. Then, the electrode was repeatedly washed running DI water to remove the excess ions and dried at 45 ℃.

Immobilization of $GO_x$ on PtNPs−PAni electrode: Glucose oxidase (glucose oxidase type II, ≥ 15000 units $g^{-1}$ solid, Sigma) was dissolved (40 mg $mL^{-1}$) in a 20 mM phosphate-buffered saline (PBS) solution. Then, 10 µL of the $GO_x$ solution was deposited onto the electrode. The electrode was maintained under ambient conditions until it was dry. A total of 10 µL of 0.1% glutaraldehyde was added to the electrode and allowed to react for 4 h to cross-link the $GO_x$ with the PtNPs−PAni hydrogel matrix. Finally, the prepared bioelectrode was washed thoroughly with 0.02 M PBS before storing it in 20 mM PBS. The PAni was rehydrated to form a hydrogel after these processes.

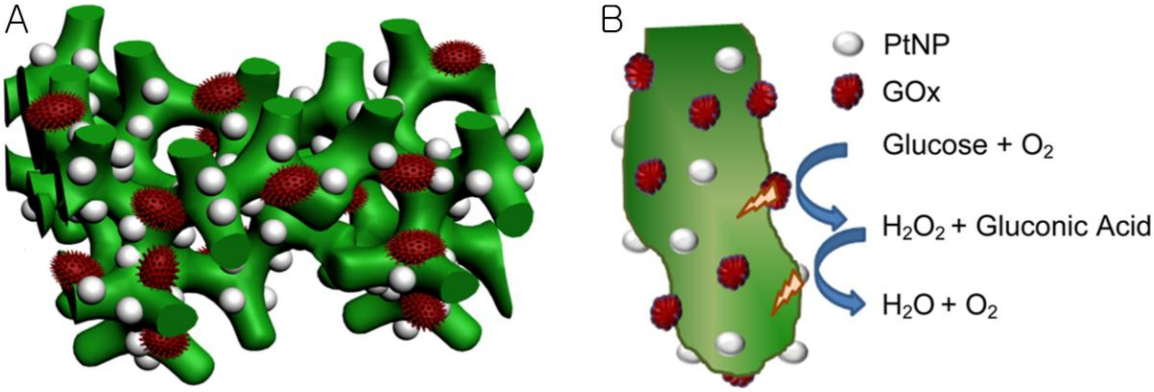

Figure 20: Schematic illustration of the 3D heterostructure of the PtNPs−PAni hydrogel.

Schematic description of the nanostructures of the 3D PtNPs−PAni electrode is shown in Fig. 20. It is clearly shown that the 3D porous nanostructures of the PAni hydrogel function as the electrically conductive framework, providing fast electron transport along the polymeric fibers three-dimensionally. Also, the porous nanostructures provide high porosity and large specific surface area, which could be beneficial to fast mass transition and large surface area in glucose solutions. Therefore, PtNPs and $GO_x$

immobilized on PAni surfaces will be better contacting with glucose solutions and efficiently detecting chemical reaction signals in the glucose solutions.

### 4.4 CHARACTERIZATIONS OF PTNPS−PANI BIOSENSORS

SEM images were taken to show the detailed nanostructures of the PtNPs−PAni hydrogel electrode. Fig. 21(A) and (B) are SEM images of PtNPs−PAni hydrogel electrode with low magnification and high magnification, respectively. The well crosslinked 3D nanoporous PAni network is shown in Fig. 21(A). The fibrous polymeric hydrogel network offers high electrical conductivity and porosity to gain high sensitivity of the composite electrode for biosensor. After zooming in, zero-dimensional PtNPs grown on PAni hydrogel fibers are clearly revealed by the rough surface of PAni hydrogel with particle-like materials coated. This indicates the PtNPs could be well immobilized and uniformly coated on PAni hydrogel matrix even after repeated washing by DI water.

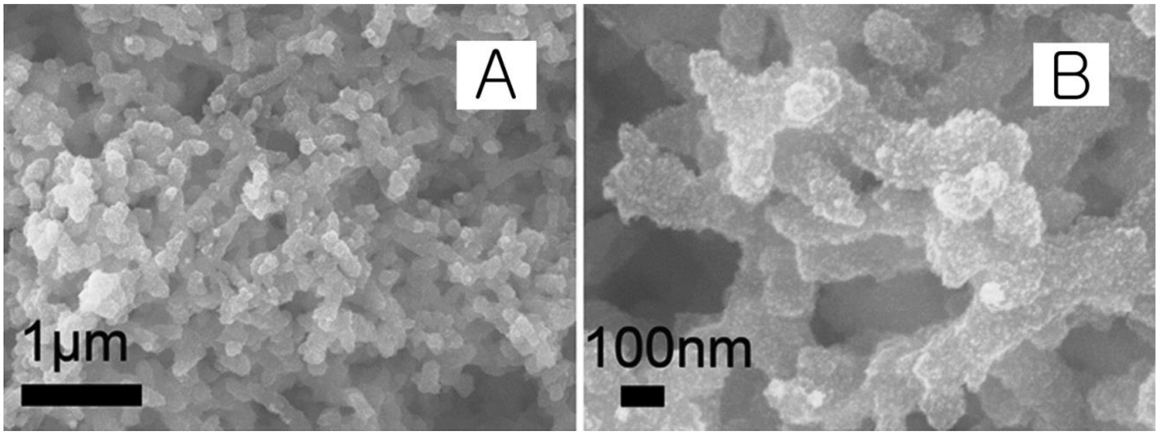

Figure 21: SEM images of PtNPs−PAni hydrogel nanocomposite. (A) 3D hierarchical nanostructures of the PtNPs−PAni hydrogel. (B) Homogeneous loading of PtNPs on the surface of the 3D PAni hydrogel network.

The mass loading density of PtNPs was qualitatively revealed in the low-magnification TEM image Fig. 22(A) and high-resolution TEM (HRTEM) image Fig. 22(B). As determined by the statistical size distribution of the PtNPs in the inset of Fig. 22(A), the PtNPs had monodispersed diameters of ca. 2 nm in average. HRTEM image in Fig. 22(B) revealed the crystalline lattices of PtNPs. The lattice spacings shown are ca. 0.23 nm and 0.20 nm, which are attributed to Pt (111) and (100) planes.[97, 98]

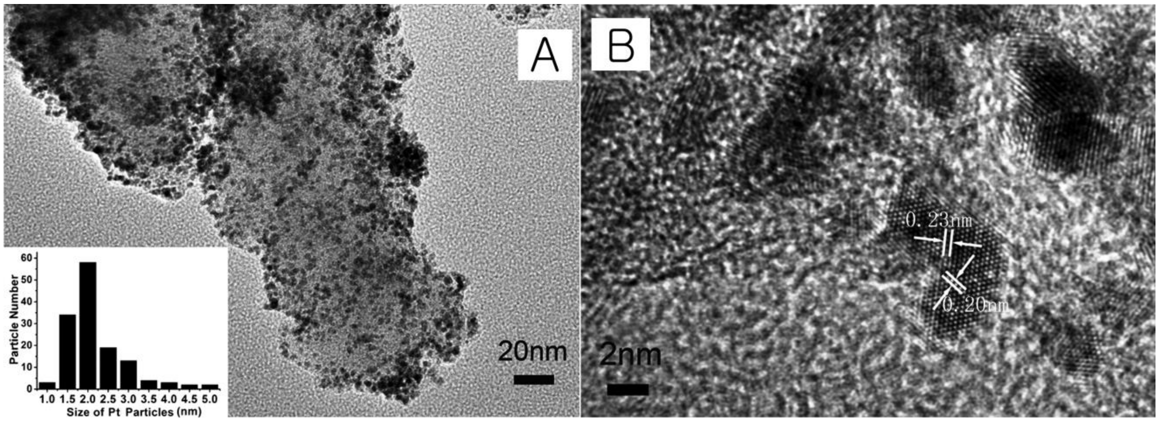

Figure 22: TEM images of PtNPs−PAni hydrogel nanocomposite. (A) mass loading density of PtNPs in the composite electrode, and (B) crystalline PtNPs on the PAni hydrogel.

To confirm the formation of PtNPs on 3D nanostructured PAni hydrogel matrix, X-ray photoelectron spectroscopy (XPS) and FTIR were conducted on the as-synthesized PtNPs−PAni hydrogel samples. XPS spectrum of Pt 4f core level region, as shown in Fig. 23(A), had three groups of subpeaks of 1, 2, and 3 labeled with binding energies of 71.1, 71.9, and 74.4 eV, respectively. The first peak was assigned to $Pt^0$,[99] while the second peak could be attributed to metallic Pt nanoparticles or $Pt^{2+}$ (byproduct), and the third peak was assigned to $Pt^{4+}$, suggesting the formation of a trace amount of $PtO_2$. The high loading of PtNPs was revealed by the atomic ratio of Pt:N (1.92:1) in Table 2. Furthermore, FTIR spectrum in Fig. 23(B) represented two characteristic peaks located at

1580 cm$^{-1}$ and 1491 cm$^{-1}$, which are attributed to the stretching vibrations of the quinoid and benzenoid rings, separately. The absorption peak near 1143 cm$^{-1}$ resulted from the N=Q=N (Q denotes quinoid ring) stretching mode, which was an indication of the electron delocalization in PAni.

Table 2: Elemental concentration of PtNPs−PAni hydrogel sample

| C1s | N1s | O1s | Cl2p | Pt4f |
|---|---|---|---|---|
| 61.30 | 8.64 | 12.51 | 0.97 | 16.59 |

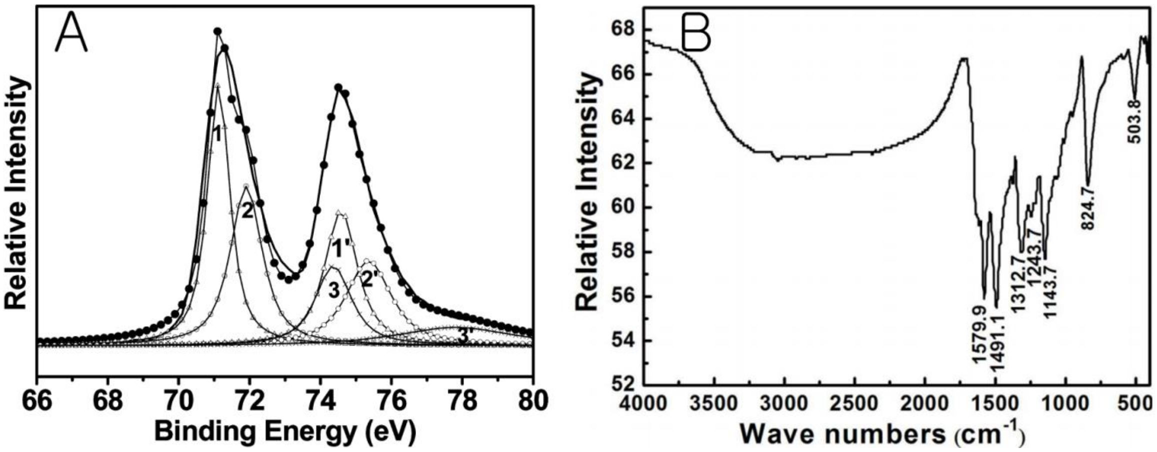

Figure 23: XPS and FTIR spectrums of PtNPs−PAni hydrogel sample. (A) Pt 4f XPS spectrum of the PtNPs−PAni hydrogel. (B) FTIR spectrum of PtNPs−PAni hydrogel electrode.

To measure the electrochemical performance of the PtNPs−PAni hydrogel biosensor, current−time responsibility was tested at 0.56 V with successive addition of glucose. Fig. 24(A) shows that the response current ramped up quickly (3 s for a 95% of steady state current in average) as soon as the addition of glucose, while still can reach up to a steady state rapidly, indicating an excellent biosensor performance of the PtNPs−PAni hydrogel composite. As shown in Fig. 24(B), in the glucose concentration range of 0.01−8 mM, the response current vs. glucose concentration plot was very close to ideal linearity, also suggesting good sensitivity and responsibility of the PtNPs−PAni hydrogel composite electrode. By calculation, sensitivity was as high as 96.1 $\mu A\cdot mM^{-1}\cdot cm^{-2}$. This is higher than all previously reported values for sensor electrodes based on composite of Pt, PAni, PPy, or multi-walled carbon nanotubes (MWCNTs), as listed in Table 3.

Table 3: Comparison of analytical performance of glucose sensors.

| Electrodes | Sensitivity ($mA\cdot cm^{-2}\cdot M^{-1}$) | Response time (s) | Linear range (mM) | Detection limit (μM) | $K_m$ (mM) | Ref. |
|---|---|---|---|---|---|---|
| $GO_x$/PPy/Pt/$Al_2O_3$ | 7.4 | < 4 | 0.5−10 | 30 | 7.01 | 100 |
| $GO_x$/MWCNTs/Pt | 52.7 | | 0−28 | 30 | | 101 |
| Nafion/$GO_x$/$Cu_2S$−MWCNTa/GC | 1.0 | | 0.01−1 | 10 | | 102 |
| $GO_x$/(Pt/C)/GC | 125 | < 5 | 0−45 | < 300 | | 103 |
| $GO_x$/Pt−DENs/PANI/CNT/Pt | 42 | 5 | 0.001−12 | 0.5 | | 104 |
| $GO_x$/Pt/MWNT−PANI/GCE | 128 | | 0.003−8.2 | 1 | 0.64 | 105 |
| $GO_x$/PAni/PAN/Pt | 67.1 | | 0.002−12 | 2 | 13 | 106 |
| GOx/AuNPs/PAni/GC | 73.25 | | 0.001−0.8 | 0.5 | | 107 |
| Pt−DENs/GOx/Pt−DENs/PAni/PSS/GC | 39.63 | 5 | 0.01−4.5 | 0.5 | | 108 |
| $GO_x$−PtNP−PAni−Pt | 96.1 | 3 | 0.01−8 | 0.7 | 2.35 | this work |

To prove the outstanding contribution of the 3D heterostructure of PtNPs−PAni hydrogel biosensor, comparison between the PtNPs−PAni hydrogel and PAni on Pt electrode was carried out. Calibration plots of current increase as a function of the $H_2O_2$ concentration of Pt electrode with PtNPs−PAni hydrogel and Pt electrode with the PAni hydrogel was shown in Fig. 25. It is obvious that the PtNPs−PAni had a much more sensitive current increase than PAni on Pt electrode, demonstrating the advantage of PtNPs−PAni's heterostructure over the PAni on Pt electrode.

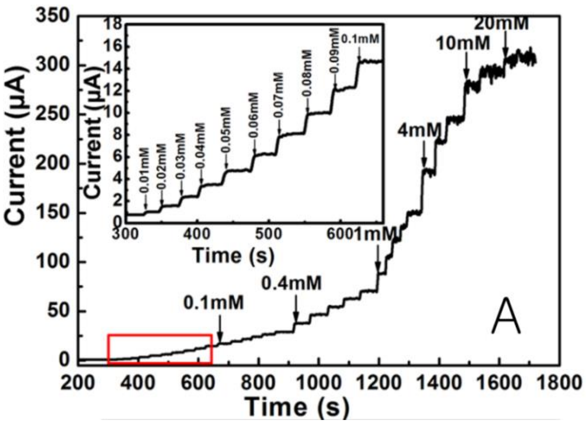

Figure 24: Electrochemical measurements for PtNPs−PAni hydrogel biosensor. (A) Amperometric response of PtNPs−PAni hydrogel electrode after successive addition of glucose in 100 mM PBS (pH = 5.6) at an applied potential of 0.56 V. Inset: the zoom-in of the red square section. (B) Calibration plot for glucose concentrations from 1μM to 80 mM.

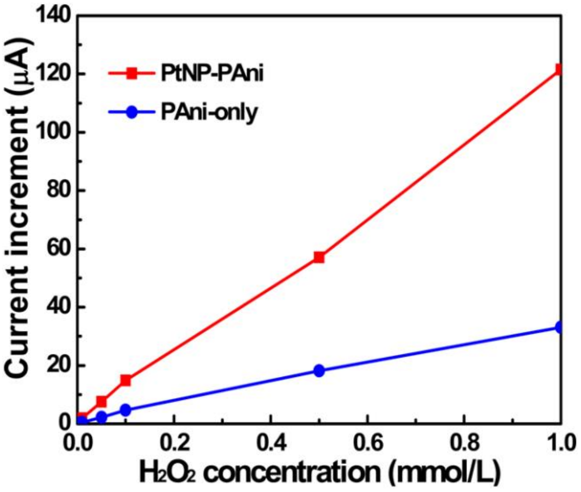

Figure 25: Calibration plots of current increase as a function of the $H_2O_2$ concentration of Pt electrode with PtNPs−PAni hydrogel and Pt electrode with the PAni hydrogel.

In conclusion, our uniquely designed 3D PtNPs−PAni hydrogel heterostructured nanocomposite demonstrated outstanding analytical performance as glucose biosensor electrodes. The novel concept and synthesis method can be extended to other types of biosensors and contribute to future potential analytical applications.

# Chapter 5: *Conclusion*

In this thesis, we proposed a novel material synthesis concept for synthesizing 3D nanostructured CPHs and studied their potentials for energy storage and glucose biosensor applications. The unique 3D hierarchical porous nanostructures offers greatly improved mass transportability. The excellent electrical conductivity and electrochemical activity of the hydrogels also provided fast electron pathways and good electric charges collecting capability. The highly porous nanostructures and hydrophilic property offered large specific surface areas to fulfill the requirement for contacting well with electrolytes or solutions. Even with ultrahigh CPHs mass loadings, the energy storage devices can still provide outstanding electrochemical performance. Moreover, stable mechanical properties enabled good physical stability for long-last operations. The flexibility of the CPHs can also afford opportunities for flexible/stretchable electronic devices.

As a key component in electronic devices, CPHs achieved by our unique synthesis method can be promisingly contributing to future scaled-up energy storage and conversion, and analytical devices fields. The major challenge of this is to optimize the synthesis procedures to be more efficient.

# Bibliography

1. Graham, N. *Chem Brit* **2001,** 37, (4), 42-44.

2. Dispenza, C.; Lo Presti, C.; Belfiore, C.; Spadaro, G.; Piazza, S. *Polymer* **2006,** 47, (4), 961-971.

3. Wang, C.; Flynn, N. T.; Langer, R. *Adv Mater* **2004,** 16, (13), 1074-+.

4. Zhang, X. B.; Pint, C. L.; Lee, M. H.; Schubert, B. E.; Jamshidi, A.; Takei, K.; Ko, H.; Gillies, A.; Bardhan, R.; Urban, J. J.; Wu, M.; Fearing, R.; Javey, A. *Nano Lett* **2011,** 11, (8), 3239-3244.

5. Zhang, L.; Wang, Z. P.; Xu, C.; Li, Y.; Gao, J. P.; Wang, W.; Liu, Y. *J Mater Chem* **2011,** 21, (28), 10399-10406.

6. Marsella, M. J.; Swager, T. M. *J Am Chem Soc* **1993,** 115, (25), 12214-12215.

7. Huang, W. S.; Humphrey, B. D.; Macdiarmid, A. G. *J Chem Soc Farad T 1* **1986,** 82, 2385-&.

8. MacDiarmid, A. G. *Synthetic Met* **1997,** 84, (1-3), 27-34.

9. Janata, J.; Josowicz, M. *Nat Mater* **2003,** 2, (1), 19-24.

10. Pan, L. J.; Yu, G. H.; Zhai, D. Y.; Lee, H. R.; Zhao, W. T.; Liu, N.; Wang, H. L.; Tee, B. C. K.; Shi, Y.; Cui, Y.; Bao, Z. N. *P Natl Acad Sci USA* **2012,** 109, (24), 9287-9292.

11. Freund, M. S.; Lewis, N. S. *P Natl Acad Sci USA* **1995,** 92, (7), 2652-2656.

12. Zhang, F. L.; Johansson, M.; Andersson, M. R.; Hummelen, J. C.; Inganas, O. *Adv Mater* **2002,** 14, (9), 662-665.

13. Baughman, R. H. *Synthetic Met* **1996,** 78, (3), 339-353.

14. Berdichevsky, Y.; Lo, Y. H. *Adv Mater* **2006,** 18, (1), 122-125.

15. Xiao, R.; Il Cho, S.; Liu, R.; Lee, S. B. *J Am Chem Soc* **2007,** 129, (14), 4483-4489.

16. Cai, Z. H.; Martin, C. R. *J Am Chem Soc* **1989,** 111, (11), 4138-4139.

17. Lee, J. I.; Cho, S. H.; Park, S. M.; Kim, J. K.; Kim, J. K.; Yu, J. W.; Kim, Y. C.; Russell, T. P. *Nano Letters* **2008,** 8, (8), 2315-2320.

18. Wu, C. G.; Bein, T. *Chem Mater* **1994,** 6, (8), 1109-1112.

19. Beck, J. S.; Vartuli, J. C.; Roth, W. J.; Leonowicz, M. E.; Kresge, C. T.; Schmitt, K. D.; Chu, C. T. W.; Olson, D. H.; Sheppard, E. W.; Mccullen, S. B.; Higgins, J. B.; Schlenker, J. L. *J Am Chem Soc* **1992,** 114, (27), 10834-10843.

20. Zhang, X. Y.; MacDiarmid, A. G.; Manohar, S. K. *Chem Commun* **2005**, (42), 5328-5330.

21. Makushok, Y. E.; Parkhutik, V. P.; Shershulskii, V. I.; Yakovlev, D. V. *Sov Electrochem* **1989,** 25, (5), 518-522.

22. Li, W. Y.; Zheng, G. Y.; Yang, Y.; Seh, Z. W.; Liu, N.; Cui, Y. *P Natl Acad Sci USA* **2013,** 110, (18), 7148-7153.

23. Cates, M. E.; Candau, S. J. *J Phys-Condens Mat* **1990,** 2, (33), 6869-6892.

24. Brahim, S.; Guiseppi-Elie, A. *Electroanal* **2005,** 17, (7), 556-570.

25. Brahim, S.; Narinesingh, D.; Guiseppi-Elie, A. *Biosens Bioelectron* **2002,** 17, (1-2), 53-59.

26. Justin, G.; Guiseppi-Elie, A. *Biomacromolecules* **2009,** 10, (9), 2539-2549.

27. Abidian, M. R.; Martin, D. C. *Adv Funct Mater* **2009,** 19, (4), 573-585.

28. Kim, D. H.; Abidian, M.; Martin, D. C. *J Biomed Mater Res A* **2004,** 71A, (4), 577-585.

29. Dai, T. Y.; Qing, X. T.; Lu, Y.; Xia, Y. Y. *Polymer* **2009,** 50, (22), 5236-5241.

30. Siddhanta, S. K.; Gangopadhyay, R. *Polymer* **2005,** 46, (9), 2993-3000.

31. Barthus, R. C.; Lira, L. M.; de Torresi, S. I. C. *J Brazil Chem Soc* **2008,** 19, (4), 630-636.

32. Gilmore, K.; Hodgson, A. J.; Luan, B.; Small, C. J.; Wallace, G. G. *Polym Gels Netw* **1994,** 2, (2), 135-143.

33. Kim, B. C.; Spinks, G. M.; Wallace, G. G.; John, R. *Polymer* **2000,** 41, (5), 1783-1790.

34. Lira, L. M.; de Torresi, S. I. C. *Electrochem Commun* **2005,** 7, (7), 717-723.

35. Abidian, M. R.; Martin, D. C. *Biomaterials* **2008,** 29, (9), 1273-1283.

36. Han, J.; Wang, L.; Guo, R. *Macromol Rapid Comm* **2011,** 32, (9-10), 729-735.

37. Abidian, M. R.; Ludwig, K. A.; Marzullo, T. C.; Martin, D. C.; Kipke, D. R. *Adv Mater* **2009,** 21, (37), 3764-3770.

38. Tang, Q. W.; Lin, J. M.; Wu, J. H.; Zhang, C. J.; Hao, S. C. *Carbohyd Polym* **2007,** 67, (3), 332-336.

39. Pan, L.; Yu, G.; Zhai, D.; Lee, H. R.; Zhao, W.; Liu, N.; Wang, H.; Tee, B. C.-K.; Shi, Y.; Cui, Y.; Bao, Z. *Proceedings of the National Academy of Sciences* **2012,** 109, (24), 9287-9292.

40. Armand, M.; Tarascon, J. M. *Nature* **2008,** 451, (7179), 652-657.

41. Gu, M.; Wang, Z.; Connell, J. G.; Perea, D. E.; Lauhon, L. J.; Gao, F.; Wang, C. *ACS Nano* **2013,** 7, (7), 6303-6309.

42. Liu, B.; Soares, P.; Checkles, C.; Zhao, Y.; Yu, G. *Nano Letters* **2013,** 13, (7), 3414-3419.

43. Miller, J. R.; Simon, P. *Science* **2008,** 321, (5889), 651-652.

44. Kötz, R.; Carlen, M. *Electrochimica Acta* **2000,** 45, (15–16), 2483-2498.

45. Augustyn, V.; Come, J.; Lowe, M. A.; Kim, J. W.; Taberna, P.-L.; Tolbert, S. H.; Abruña, H. D.; Simon, P.; Dunn, B. *Nat Mater* **2013,** 12, (6), 518-522.

46. Zhang, L. L.; Zhou, R.; Zhao, X. S. *Journal of Materials Chemistry* **2010,** 20, (29), 5983-5992.

47. Zhu, Y.; Murali, S.; Stoller, M. D.; Ganesh, K. J.; Cai, W.; Ferreira, P. J.; Pirkle, A.; Wallace, R. M.; Cychosz, K. A.; Thommes, M.; Su, D.; Stach, E. A.; Ruoff, R. S. *Science* **2011,** 332, (6037), 1537-1541.

48. Wang, Y.; Shi, Z.; Huang, Y.; Ma, Y.; Wang, C.; Chen, M.; Chen, Y. *The Journal of Physical Chemistry C* **2009,** 113, (30), 13103-13107.

49. Chen, Z.; Wen, J.; Yan, C.; Rice, L.; Sohn, H.; Shen, M.; Cai, M.; Dunn, B.; Lu, Y. *Advanced Energy Materials* **2011,** 1, (4), 551-556.

50. Gao, W.; Singh, N.; Song, L.; Liu, Z.; Reddy, A. L. M.; Ci, L.; Vajtai, R.; Zhang, Q.; Wei, B.; Ajayan, P. M. *Nat Nano* **2011,** 6, (8), 496-500.

51. Pandolfo, A. G.; Hollenkamp, A. F. *Journal of Power Sources* **2006,** 157, (1), 11-27.

52. Xia, H.; Meng, Y. S.; Yuan, G.; Cui, C.; Lu, L. *Electrochemical and Solid-State Letters* **2012,** 15, (4), A60-A63.

53. Bi, R.-R.; Wu, X.-L.; Cao, F.-F.; Jiang, L.-Y.; Guo, Y.-G.; Wan, L.-J. *The Journal of Physical Chemistry C* **2010,** 114, (6), 2448-2451.

54. Ryu, I.; Yang, M.; Kwon, H.; Park, H. K.; Do, Y. R.; Lee, S. B.; Yim, S. *Langmuir* **2014,** 30, (6), 1704-1709.

55. Balan, B. K.; Chaudhari, H. D.; Kharul, U. K.; Kurungot, S. *RSC Advances* **2013,** 3, (7), 2428-2436.

56. Chen, S.; Zhu, J.; Wu, X.; Han, Q.; Wang, X. *ACS Nano* **2010,** 4, (5), 2822-2830.

57. Liu, K.-y.; Zhang, Y.; Zhang, W.; Zheng, H.; Su, G. *Transactions of Nonferrous Metals Society of China* **2007,** 17, (3), 649-653.

58. Ye, C.; Lin, Z. M.; Hui, S. Z. *Journal of The Electrochemical Society* **2005,** 152, (6), A1272-A1278.

59. Ghodbane, O.; Pascal, J.-L.; Favier, F. *ACS Applied Materials & Interfaces* **2009,** 1, (5), 1130-1139.

60. Lu, X.; Zhai, T.; Zhang, X.; Shen, Y.; Yuan, L.; Hu, B.; Gong, L.; Chen, J.; Gao, Y.; Zhou, J.; Tong, Y.; Wang, Z. L. *Adv Mater* **2012,** 24, (7), 938-944.

61. Liu, Y.; He, D.; Wu, H.; Duan, J. *Integrated Ferroelectrics* **2013,** 144, (1), 118-126.

62. Lee, J. W.; Hall, A. S.; Kim, J.-D.; Mallouk, T. E. *Chem Mater* **2012,** 24, (6), 1158-1164.

63. Gao, H.; Xiao, F.; Ching, C. B.; Duan, H. *ACS Applied Materials & Interfaces* **2012,** 4, (12), 7020-7026.

64. Chen, Z.; Augustyn, V.; Wen, J.; Zhang, Y.; Shen, M.; Dunn, B.; Lu, Y. *Adv Mater* **2011,** 23, (6), 791-795.

65. Wee, G.; Soh, H. Z.; Cheah, Y. L.; Mhaisalkar, S. G.; Srinivasan, M. *Journal of Materials Chemistry* **2010,** 20, (32), 6720-6725.

66. Lee, H. Y.; Goodenough, J. B. *Journal of Solid State Chemistry* **1999,** 148, (1), 81-84.

67. Saravanakumar, B.; Purushothaman, K. K.; Muralidharan, G. *ACS Applied Materials & Interfaces* **2012,** 4, (9), 4484-4490.

68. Yang, Y.; Kim, D.; Yang, M.; Schmuki, P. *Chem Commun* **2011,** 47, (27), 7746-7748.

69. Lu, X.; Wang, G.; Zhai, T.; Yu, M.; Gan, J.; Tong, Y.; Li, Y. *Nano Letters* **2012,** 12, (3), 1690-1696.

70. Wang, Q.; Wen, Z. H.; Li, J. H. *Adv Funct Mater* **2006,** 16, (16), 2141-2146.

71. Wang, Q.; Wen, Z.; Li, J. *Journal of Nanoscience and Nanotechnology* **2007,** 7, (9), 3328-3331.

72. Dubal, D. P.; Fulari, V. J.; Lokhande, C. D. *Microporous and Mesoporous Materials* **2012,** 151, (0), 511-516.

73. Vijayakumar, S.; Nagamuthu, S.; Muralidharan, G. *ACS Applied Materials & Interfaces* **2013,** 5, (6), 2188-2196.

74. Yu, G.; Hu, L.; Liu, N.; Wang, H.; Vosgueritchian, M.; Yang, Y.; Cui, Y.; Bao, Z. *Nano Letters* **2011,** 11, (10), 4438-4442.

75. Yu, G.; Hu, L.; Vosgueritchian, M.; Wang, H.; Xie, X.; McDonough, J. R.; Cui, X.; Cui, Y.; Bao, Z. *Nano Letters* **2011,** 11, (7), 2905-2911.

76. Peng, L.; Peng, X.; Liu, B.; Wu, C.; Xie, Y.; Yu, G. *Nano Letters* **2013,** 13, (5), 2151-2157.

77. Yu, G.; Xie, X.; Pan, L.; Bao, Z.; Cui, Y. *Nano Energy* **2013,** 2, (2), 213-234.

78. Wu, C.; Lu, X.; Peng, L.; Xu, K.; Peng, X.; Huang, J.; Yu, G.; Xie, Y. *Nat Commun* **2013,** 4.

79. Zheng, J. P.; Cygan, P. J.; Jow, T. R. *Journal of The Electrochemical Society* **1995,** 142, (8), 2699-2703.

80. Konwer, S.; Dolui, S. K. *Mater Chem Phys* **2010,** 124, (1), 738-743.

81. Lu, X. H.; Wang, G. M.; Zhai, T.; Yu, M. H.; Xie, S. L.; Ling, Y. C.; Liang, C. L.; Tong, Y. X.; Li, Y. *Nano Lett* **2012,** 12, (10), 5376-5381.

82. Zhang, L. L.; Zhao, X.; Stoller, M. D.; Zhu, Y. W.; Ji, H. X.; Murali, S.; Wu, Y. P.; Perales, S.; Clevenger, B.; Ruoff, R. S. *Nano Lett* **2012,** 12, (4), 1806-1812.

83. Meng, F. H.; Ding, Y. *Adv Mater* **2011,** 23, (35), 4098-4102.

84. Clark, L. C.; Lyons, C. *Ann Ny Acad Sci* **1962,** 102, (1), 29-&.

85. Guilbault, G. G.; Lubrano, G. J. *Analytica Chimica Acta* **1973,** 64, (3), 439-455.

86. Schlapfe.P; Mindt, W.; Racine, P. *Clin Chim Acta* **1974,** 57, (3), 283-289.

87. Shichiri, M.; Kawamori, R.; Yamasaki, Y.; Hakui, N.; Abe, H. *Lancet* **1982,** 2, (8308), 1129-1131.

88. Frew, J. E.; Hill, H. A. O. *Anal Chem* **1987,** 59, (15), A933-&.

89. Matthews, D.; Holman, R. *Lancet* **1987,** 1, (8543), 1205-1206.

90. Degani, Y.; Heller, A. *J Phys Chem-Us* **1987,** 91, (6), 1285-1289.

91. Schmidtke, D. W.; Freeland, A. C.; Heller, A.; Bonnecaze, R. T. *P Natl Acad Sci USA* **1998,** 95, (1), 294-299.

92. Albery, W. J.; Bartlett, P. N.; Craston, D. H. *J Electroanal Chem* **1985,** 194, (2), 223-235.

93. Khan, G. F.; Ohwa, M.; Wernet, W. *Anal Chem* **1996,** 68, (17), 2939-2945.

94. Palmisano, F.; Zambonin, P. G.; Centonze, D.; Quinto, M. *Anal Chem* **2002,** 74, (23), 5913-5918.

95. Cenas, N. K.; Kulys, J. J. *Bioelectroch Bioener* **1981,** 8, (1), 103-113.

96. Zhai, D. Y.; Liu, B. R.; Shi, Y.; Pan, L. J.; Wang, Y. Q.; Li, W. B.; Zhang, R.; Yu, G. H. *Acs Nano* **2013,** 7, (4), 3540-3546.

97. Wu, J. M.; Yin, L. W. *Acs Applied Materials & Interfaces* **2011,** 3, (11), 4354-4362.

98. Guo, S. J.; Dong, S. J.; Wang, E. K. *Small* **2009,** 5, (16), 1869-1876.

99. Jin, T.; Zhou, Y.; Mains, G. J.; White, J. M. *J Phys Chem-Us* **1987,** 91, (23), 5931-5937.

100. Ekanayake, E. M. I. M.; Preethichandra, D. M. G.; Kaneto, K. *Biosens Bioelectron* **2007,** 23, (1), 107-113.

101. Xie, J. N.; Wang, S.; Aryasomayajula, L.; Varadan, V. K. *Nanotechnology* **2007,** 18, (6).

102. Lee, H.; Yoon, S. W.; Kim, E. J.; Park, J. *Nano Letters* **2007,** 7, (3), 778-784.

103. Ammam, M.; Easton, E. B. *Sensor Actuat B-Chem* **2011,** 155, (1), 340-346.

104. Xu, L. H.; Zhu, Y. H.; Yang, X. L.; Li, C. Z. *Mat Sci Eng C-Bio S* **2009,** 29, (4), 1306-1310.

105. Zhong, H. A.; Yuan, R.; Chai, Y. Q.; Li, W. J.; Zhong, X.; Zhang, Y. *Talanta* **2011,** 85, (1), 104-111.

106. Xue, H. G.; Shen, Z. Q.; Li, C. M. *Biosens Bioelectron* **2005,** 20, (11), 2330-2334.

107. Xian, Y. Z.; Hu, Y.; Liu, F.; Xian, Y.; Wang, H. T.; Jin, L. T. *Biosens Bioelectron* **2006,** 21, (10), 1996-2000.

108. Xu, L. H.; Zhu, Y. H.; Tang, L. H.; Yang, X. L.; Li, C. Z. *J Appl Polym Sci* **2008,** 109, (3), 1802-1807.